

THESIS

ANALYSIS OF CuCl THIN-FILM DEPOSITION AND GROWTH BY CLOSE-SPACE
SUBLIMATION

Submitted by

Anthony Nicholson

Department of Mechanical Engineering

In partial fulfillment of the requirements

For the Degree of Master of Science

Colorado State University

Fort Collins, Colorado

Spring 2016

Master's Committee:

Advisor: Walajabad Sampath

Hiroshi Sakurai
James Sites

Copyright by Anthony Nicholson 2016

All Rights Reserved

ABSTRACT

ANALYSIS OF CuCl THIN-FILM DEPOSITION AND GROWTH BY CLOSE-SPACE SUBLIMATION

There is a growing need to implement high-fidelity, scalable computational models to various thin-film photovoltaic industries. Developing accurate simulations that govern the thermal and species-transport diffusion characteristics within thin-film manufacturing processes will lead to better predictions of thin-film uniformity at varied deposition conditions that ultimately save time, money, and resources.

Thin-film deposition and growth of Copper I Chloride (CuCl) by the Close-Space Sublimation (CSS) process was investigated in an extensive range of operating and thermal conditions. A simulation model based on the ANSYS[®] FLUENT solver platform was developed to encompass the kinetic behavior of the CuCl species within the CSS domain while predicting the growth rate at varied system parameters. Surface physics associated with the process, notably sublimation and adsorption, were studied, quantified, and applied to the continuum-based thin-film growth model. Experimentation of CuCl thin-film growth was performed across a range of substrate and source temperatures as means for verification of the model's computational accuracy. Furthermore, characterization of the inherent growth mode exhibited by CuCl was studied in conjunction with simulation and experimental tasks.

It was concluded that the simulation model provided predictions for the CuCl thickness accuracy as a function of temperature within the range of typical CSS conditions. Equally important was the elucidation of the CuCl growth mechanism, which displays a Volmer-Weber growth mode on the Fluorine-doped Tin Oxide coated layer of the substrate. Such

knowledge along with the current modeling capabilities will be useful in extending the computational method to predicting the non-uniformities present in CuCl and other thin-film depositions.

ACKNOWLEDGEMENTS

I would like to first thank my God Jehovah for the loving guidance and blessings provided throughout my life. With any struggles I face, He is always there to sustain me. I am deeply thankful to my parents for their encouragement and continuous support in my endeavors. They have sacrificed a lot to raise me into the person I am today; I truly appreciate it. An extended thanks goes out to my advisor Dr. Sampath and committee members for their expertise and willingness to help me understand tough concepts within my graduate studies. Furthermore, I am deeply grateful for Kurt Barth's assistance in pointing me in the right direction regarding research tasks and deliverables. I am also grateful toward Pat McCurdy and Jack Clark, both of whom have been a major help in teaching me various characterization techniques and instrument operation with much patience. For all others I forgot to mention, I am humbled by your willingness to assist me when I needed it most. Thank you.

This material is based upon work supported by the National Science Foundation Graduate Fellowship Research Program under Grant No. DGE-1321845 Amend 3. This research study is also in direct partnership with the Accelerating Innovation Research Technology Translation project and was originally a project under the Industry/University Corporative Research Center.

This thesis is typeset in \LaTeX using a document class designed by Leif Anderson.

TABLE OF CONTENTS

ABSTRACT	ii
ACKNOWLEDGEMENTS.....	iv
LIST OF TABLES.....	vii
LIST OF FIGURES.....	viii
CHAPTER 1. INTRODUCTION.....	1
1.1. IMPORTANCE OF SIMULATION MODELING.....	1
1.2. BACKGROUND OF CuCl IN THIN-FILM PV APPLICATIONS.....	4
1.3. IMPORTANCE OF THESIS WORK.....	4
CHAPTER 2. THEORY.....	7
2.1. PRIMARY KINETIC PROCESSES.....	7
2.1.1. SUBLIMATION.....	7
2.1.2. ADSORPTION.....	10
2.1.3. GROWTH MECHANISMS.....	12
2.2. SPECIES MODELING THEORY.....	13
CHAPTER 3. EXPERIMENTAL/SIMULATION METHODS.....	21
3.1. CSS TECHNIQUE IN CuCl THIN-FILM GROWTH.....	21
3.2. CuCl MASS-LOSS EXPERIMENT.....	25
3.3. CuCl THICKNESS MEASUREMENT TECHNIQUE.....	27
3.3.1. FORMER METHODS.....	27
3.3.2. CURRENT METHOD.....	28
3.4. SIMULATION METHOD.....	32

CHAPTER 4. RESULTS/DISCUSSION	36
4.1. FULL-WELL DEPOSITION	36
4.2. SINGLE-WELL DEPOSITION	43
4.3. SEM/EDS ANALYSIS	46
4.3.1. SEM ANALYSIS	47
4.3.2. EDS ANALYSIS	48
4.3.3. SUMMARY	49
CHAPTER 5. CONCLUSION/FUTURE WORK	56
5.1. CONCLUSION	56
5.2. FUTURE WORK	59
BIBLIOGRAPHY	61
APPENDIX A. TECHNIQUE VERIFICATION	65
A.1. HYDROCHLORIC ACID ETCHING ON TCO	65
A.2. XPS ARGON ION BEAM SPUTTERING ON CuCl/TCO LAYERS	65
APPENDIX B. CSS DOMAIN THERMAL UNIFORMITY VERIFICATION	68
APPENDIX C. SUBLIMATION RATE PRESSURE DEPENDENCE	73

LIST OF TABLES

4.1	Full-well CuCl CSS deposition runs in the ARDS	37
4.2	Simulated CuCl impingement rate Φ [nm/s] at each source temperature	37
4.3	S curve fitted parameters used for each source temperature	39
4.4	Single-well CuCl CSS deposition runs in the ARDS	43
A.1	Average TCO crater depth before and after HCl etching at varied Ar ⁺ sputtering times	65

LIST OF FIGURES

1.1	Analogy of the three-way process interaction between theory, experiment, and simulation	2
1.2	Original and modified CdS source contour plots demonstrating the improved deposition rate uniformity across the substrate (image taken with permission from [6])	3
1.3	(a) Typical CdTe device structure made in current CSS process (red layer marks the Cu-doped region in CdTe). (b) J-V curves of intentionally Cu-doped vs. undoped CdTe cell devices (image taken with permission from [11])	5
2.1	CuCl sublimation within the bottom source. CuCl partial pressure eventually reaches saturation as long as the surface temperatures within the pocket are equal and no leaks are present while the shutter is covering the source pocket. (d) is a zoomed representation of one of the bottom source wells from (c) when the evaporation rate is equal to the condensation rate at the solid-vapor interface.....	9
2.2	CuCl adsorption occurring at the substrate. Adsorption is dictated by a sticking coefficient on a given surface that can be attributed to one of the three systematic growth mechanisms.....	11
2.3	Schematic demonstrating the significance of the CuCl sticking coefficient.....	13
2.4	Primary growth modes displayed by various thin-films. Such modes are dependent on the surface energies of the substrate and adsorbed overlayer.....	14
2.5	Schematic of species transport calculation throughout entire mesh domain. (a) Sublimation kinetic rate is enabled to allow FLUENT to compute and store the mass fraction Y for CuCl in the cell-centers that are compared to surrounding	

	values that determine whether a solution for $\nabla \vec{J}_i = R_i$ has converged. (c) After convergence, the 1 st adjacent cell-center layer to the substrate impingement face-centers will influence the impingement rate calculated to obtain a simulated CuCl thickness.....	18
2.6	Example of CuCl mass fraction calculated in simulation model based off of R_1 (sublimation) at the bottom source and R_2 (impingement) at the substrate.....	19
3.1	(a) Full-well and (b) single-well depositions in the ARDS. Upon further analysis, the distinct color difference between experiments indicated whether the CuCl powder continuously sublimated (darker) or not (lighter) after completing all deposition runs.....	23
3.2	Illustration of the substrate temperature calculation.....	25
3.3	Temperature plot of the 18-hr sublimation experiments ran at CuCl bottom source temperature = 210, 220, and 230°C.....	27
3.4	(a) Contour representation and (b) thickness profile plot of CuCl after DI and Acetone was dripped on substrate. Generalizations of CuCl thin-film growth with respect to temperature could not be made using this inconsistent method, thus a new technique was devised for measuring CuCl thicknesses.	29
3.5	(a) Expected CuCl crater locations and (b) typical crater locations on a TEC-12D substrate. The substrate is divided into 3 x 3 samples that are labeled by position values 1-9. Only positions 3, 5, and 7 are used for crater etching.....	30
3.6	Schematic of CuCl/TCO crater formation during Ar ⁺ sputtering process.....	30
3.7	(a) Areal representation of a typical CuCl crater measured with SWLI. (b) Test and reference mask used within CuCl crater depth analysis, where the test mask	

	is the entire area shaded in orange (purple) and the reference masks are the long rectangular boxes used as leveling planes for each data set.....	32
3.8	CuCl (a) mesh model used during FLUENT simulation, and (b) contour example when kinetic rates were activated to determine the CuCl mass fraction throughout the pocket. This example was performed at a substrate and source temperature of 180.6°C and 210°C, respectively. (c) Specified kinetic rates R_1 and R_2 at the bottom well source and top substrate wall boundaries, respectively.	34
3.9	Examples of full well and single well simulation deposition rates. Along the black dotted line are where 150 points were mapped across the substrate diagonal to measure the deposition rate profile from position 3 to 7 (referenced by Figure 3.5a) on the substrate for comparison to experimental results. These two examples were modeled at a substrate and source temperature of 191.7°C and 210°C, respectively.	35
4.1	S curve fits at each source temperature using equation 4.1.....	39
4.2	Full-well deposition experimental and simulated thicknesses at a source temperature of (a) 210, (b) 200, and (c) 190°C.....	40
4.3	Single-well deposition experimental and simulated thicknesses at a source temperature of (a) 210, (b) 200, and (c) 190°C.....	44
4.4	SEM images for source temperature = 210°C and substrate temperature = (a) 180.6, (b) 187.9, (c) 191.7, (d) 195.4, and (e) 210.7°C. (f) SEM image of TCO layer only on TEC-12D substrate (no deposition) as a visual comparison with (e). The scale on the bottom right of each image is 100 nm.	50

4.5	SEM images for source temperature = 200°C and substrate temperature = (a) 177.9, (b) 181.0, and (c) 185.3°C. The scale on the bottom right of each image is 100 nm.	51
4.6	SEM images for source temperature = 200°C and substrate temperature = (a) 177.9, (b) 181.0, and (c) 185.3°C. The scale on the bottom right of each image is 100 nm.	52
4.7	EDS images for source temperature = 210°C and substrate temperature = (a) 180.6, (b) 187.9, (c) 191.7, (d) 195.4, and (e) 210.7°C. The scale at the bottom left of each image is 0.5 μm	53
4.8	EDS images for source temperature = 200°C and substrate temperature = (a) 177.9, (b) 181.0, and (c) 185.3°C. The scale at the bottom left of each image is 0.5 μm	54
4.9	EDS images for source temperature = 190°C and substrate temperature = (a) 172.1, (b) 175.3, and (c) 179.4°C. The scale at the bottom left of each image is 0.5 μm	55
A.1	TCO crater depth while unetched and etched with HCl	66
A.2	XPS on CuCl/TCO Crater	67
B.1	(a) Side and (b) orthogonal view of the TC locations on the CuCl bottom source and side shielding.....	69
B.2	Thermocouple Data in CuCl Domain	70

B.3	(a) Full and (b) close-up contour plot of the CuCl domain when top heater = 166.3°C and bottom source = 192.5°C. The substrate temperature appears to be uniform according to the thermal model.....	71
B.4	Substrate temperature plot from the thermal model analysis	72

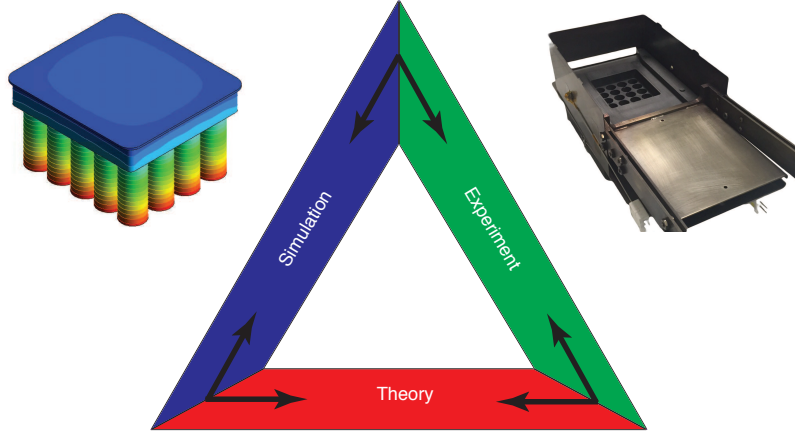
CHAPTER 1

INTRODUCTION

1.1. IMPORTANCE OF SIMULATION MODELING

The demand for computational methods and simulations in manufacturing have been steadily increasing over the years. The common three-way paradigm analogy between experiment, theory, and simulation [1, 2] shown in Figure 1.1 demonstrates the importance of computational modeling in research of real-world applications and processes. Each component in the paradigm shares knowledge with the other in order to gain a better understanding of the overall process, which is why simulation can maintain its role as a separate entity from theory and experiment. Since the beginning of rapid advancements in integrated circuitry [3], computational capabilities have proliferated over the years to the point where simulation modeling is faster and economically feasible when applied to industrial design methods. That is why in recent years many technological industries are looking for robust simulation tools that can substantially improve manufacturing processes. The benefits of using simulation within industrial sectors include numerous savings in production costs and time, reducing operation risks [4], and providing an avenue for rapid virtual prototyping. By developing high fidelity models with visual and animated capabilities [5], detailed understanding of the manufacturing process is attainable for better design decisions.

In spite of this push toward simulation for industrial processes, there are no current standard methods of implementing thin-film deposition models that are both computationally accurate and versatile within photovoltaic (PV) industrial manufacturing systems. Such a void in simulation leads to costly “trial and error” design and processing decisions that



$$k_r = A_r \cdot T^\beta \cdot \exp\left(\frac{-E}{RT}\right)$$

FIGURE 1.1. Analogy of the three-way process interaction between theory, experiment, and simulation

impede the progress toward optimal solutions in thin-film deposition, most notably the thin-film uniformity across large PV modules. Furthermore, the absence of simulation prevents further system design exploration since experiments are only limited to an understanding of the current system capabilities rather than finding other alternatives to improve the PV manufacturing process. Therefore developing a standard simulation method in the thin-film and PV industries will help give a detailed understanding of the overall manufacturing process that will lead to better design decisions. These accurate simulations can be applied to various processing conditions without running the risk of compromising the current deposition tool or its thin-film materials. Simulation modeling is also scalable and thus can be expanded to both small and large-scale PV production lines that cannot be done as easily with experiments alone. Inclusion of the simulation component in the research methodology of thin-film deposition will ultimately save manufacturing time in optimizing thin-film uniformity as well as costs and resources associated with the deposition process.

One example of the benefits seen locally within deposition modeling has been the investigation of Cadmium Sulfide (CdS) deposition during a processing technique known as Close Space Sublimation (CSS) [6]. Transient simulations on Cd and S₂ species diffusion through the control volume of the CdS bottom source revealed pre-existing non-uniformities of several percent across the deposition area using the original CdS source geometry. Switching to a deeper pocket with more shallow wells led to a much more uniform deposition across the same area (Figure 1.2) during CSS operation that was verified with experimental results. Such results indicate the usefulness simulation modeling has on determining uniformities within thin-film deposition techniques and how new predictive solutions can be extended to other materials such as CuCl. The next section will provide background information on CuCl and its function as a doping mechanism of the Cadmium Telluride (CdTe) absorber layer. It will hopefully become evident as to why CuCl adsorption uniformity plays such a vital role to the efficiency of CdTe solar cells made at CSU and how thin-film growth analysis from both an experimental and computational standpoint can assist in understanding the inherent mechanism of CuCl thin-film growth.

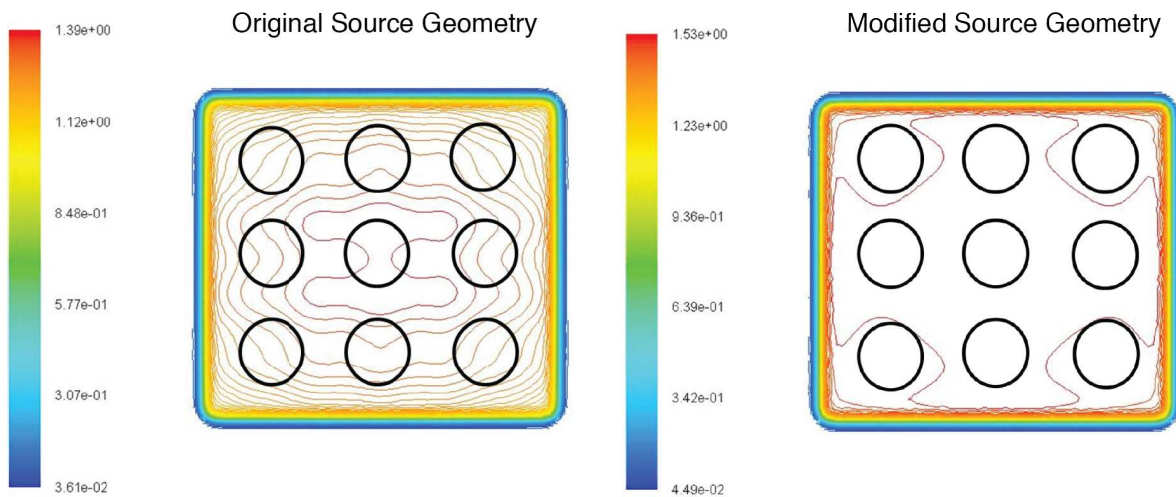


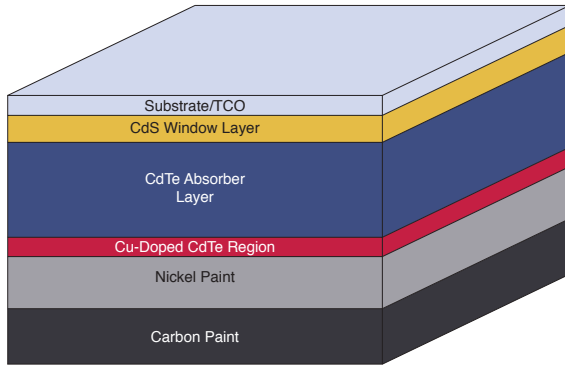
FIGURE 1.2. Original and modified CdS source contour plots demonstrating the improved deposition rate uniformity across the substrate (image taken with permission from [6])

1.2. BACKGROUND OF CuCl IN THIN-FILM PV APPLICATIONS

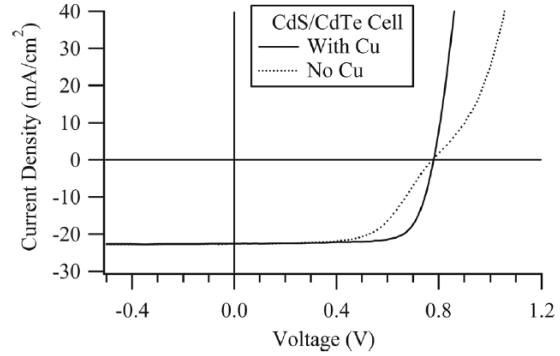
CuCl is classified as a semiconducting material that displays useful properties when applied to thin-film PV deposition and has been studied for many decades. Previous research conducted on CuCl as an evaporant to form Cu₂S on a CdS layer [7, 8] aided in a PV fabrication process that produced solar cell efficiencies of < 10%. However, dramatic efficiency losses due to, at least in part, uncontrolled stoichiometric instabilities in the films [9] prevented these PV materials from being competitive in the energy market. Over time, much of the solar cell community continued to look for new arrangements and semiconducting materials to achieve higher efficiencies. To date, CuCl is primarily used as a dopant for various thin-film PV devices, most notably CdTe. The device structure of a baseline CdTe PV device shown in Figure 1.3a illustrates where CuCl is typically introduced in the fabrication process. Here at CSU, CuCl is sublimated via CSS as a precursor state and is deposited onto the CdTe absorber layer. After deposition, annealing takes place on the substrate, during which Cu diffuses into the CdTe layer and forms shallow donor regions [10] that aid in the solar cell efficiency. Figure 1.3b [11] depicts the J-V curves when CdTe is intentionally Cu-doped vs an undoped cell. It is evident that the PV device with Cu included resembles a diode-like behavior that results in higher efficiency while the cell with no Cu develops unfavorable kinks in the curve. There is a limit to beneficial effects of Cu doping, however. It is well known among the CdTe PV community that too much Cu doping can cause cell degradation that affects the open-circuit voltage V_{oc} in the cell and lowers device performance [12, 13].

1.3. IMPORTANCE OF THESIS WORK

In order to help achieve a highly uniform Cu doping process, an overall understanding of CuCl deposition in CSS must be developed. Such a task presents quite a number of challenges



(a)



(b)

FIGURE 1.3. (a) Typical CdTe device structure made in current CSS process (red layer marks the Cu-doped region in CdTe). (b) J-V curves of intentionally Cu-doped vs. undoped CdTe cell devices (image taken with permission from [11])

for many areas related to continuum-based simulation modeling and experimentation. In order to begin simulating the deposition environment, a keen understanding of the theory involved within CSS needs to be established so that connections can be made between system parameters and how they affect both sublimation and adsorption of CuCl. After this initial step, a thin-film growth model can be built that encompasses such kinetic processes across a wide range of system parameters. The collection of CuCl material properties as a function of such parameters is accomplished as well. The simulation model finally requires some type of experimental verification of its computational accuracy. If the model does not fully represent the experimental results with a high degree of accuracy, then refinement of the modeling setup must be done. Refinement may be repeated many times before a well-behaved solution is obtained that can accurately predict thin-film deposition conditions. The research presented here follows this multistep process in regards to CuCl thin-film growth

on Fluorine-doped Tin Oxide (FTO), or “Transparent Conductive Oxide” (TCO), coated substrates (both terms are used interchangeably throughout this work). Equally important in this study is the characterization of the CuCl thin-films, which elucidates some key growth mode characteristics exhibited by CuCl during CSS. It is hoped that the efforts made in this work can eventually assist in controlling the amount of CuCl adsorbing to the CdTe layer and potentially lead to a more uniform back contact that can maintain higher CdTe PV efficiencies.

CHAPTER 2

THEORY

The physical phenomena associated with CSS can be separated into two underlying processes: 1) sublimation of a particular bulk species (i.e. CuCl) within the pocket domain, and 2) adsorption of the resulting vapor species on a substrate layer. Numerous factors such as pressure, temperature, and surface preparation influence the kinetic rates of both processes and add much complexity to the resulting growth overlayers. Furthermore, several kinetic processes [14] involved with thin-film growth (many of which are beyond the scope of this work) are governed by probabilistic interactions that require ab initio molecular dynamics [15] to fully comprehend. This chapter simply focuses on distinguishing the characteristics of sublimation and adsorption from a theoretical perspective while considering other important terms that correct for the deviation found in actual thin-film growth rates. The chapter will also explain the theory behind finite-rate species modeling and how ANSYS® FLUENT uses it to obtain the CuCl simulated deposition thickness.

2.1. PRIMARY KINETIC PROCESSES

2.1.1. SUBLIMATION. Sublimation is defined as the phase transition from a solid state to a vapor state for a given material. The rate of sublimation within this study was defined in the form of the Antoine equation where T is temperature and B and C are arbitrary constants (equation 2.1). An alternative expression for the sublimation rate that ANSYS® FLUENT recognizes is known as the Arrhenius rate expression (equation 2.2). Both expressions are defined as follows:

$$(2.1) \quad R_{sublimation} = \frac{B}{T} + C$$

$$(2.2) \quad R_{sublimation} = A \cdot \exp\left(\frac{-E}{RT}\right)$$

In equation 2.2, A is the pre-exponential factor, E denotes the activation energy, T is temperature of the source [K], and R is the universal gas constant [8314 J/kgmol-K]. Although not explicitly stated in equation 2.2, sublimation can be influenced by pressures in the system that span the diffusion-limited regime ($\approx > 50$ mTorr) [16]. However, the normal operating pressure within the CSS deposition system is at 40 mTorr, which is less than the diffusion-limited case. Furthermore, the controlled flow of ambient mixed-gas (98% N₂, 2% O₂) is maintained at this pressure throughout the entire system operation. Therefore it was assumed that the sublimation rate obtained from this particular study was independent of operating pressure and thus only varied with source temperature. This was done to focus solely on an investigation of the thermal aspects of the system rather than coupling it with operating pressure dependencies.

Figures 2.1a - 2.1d provide schematics of CuCl sublimation within the CSS chamber as the CuCl partial pressure increases to saturation within the source pocket geometry at a given source temperature T_{source} . Sublimation begins with a few CuCl molecules having enough thermal energy to break their solids bonds to become vapor (Figure 2.1a). Over time, a CuCl partial pressure continues to build within the pocket since the evaporation rate is greater than the condensation rate at the solid-gas interface (Figure 2.1b). At saturation (Figure 2.1c), equilibrium vapor pressure of CuCl is achieved since the evaporation rate is now equal to the condensation rate (Figure 2.1d). Therefore no further sublimation occurs in the pocket [17]. Once the substrate enters the source domain at temperature $T_{substrate} < T_{source}$, deposition will occur due to the CuCl gas molecules directly adjacent to the the substrate surface adsorbing to it (Figure 2.2). The vapor pressure will no longer be in

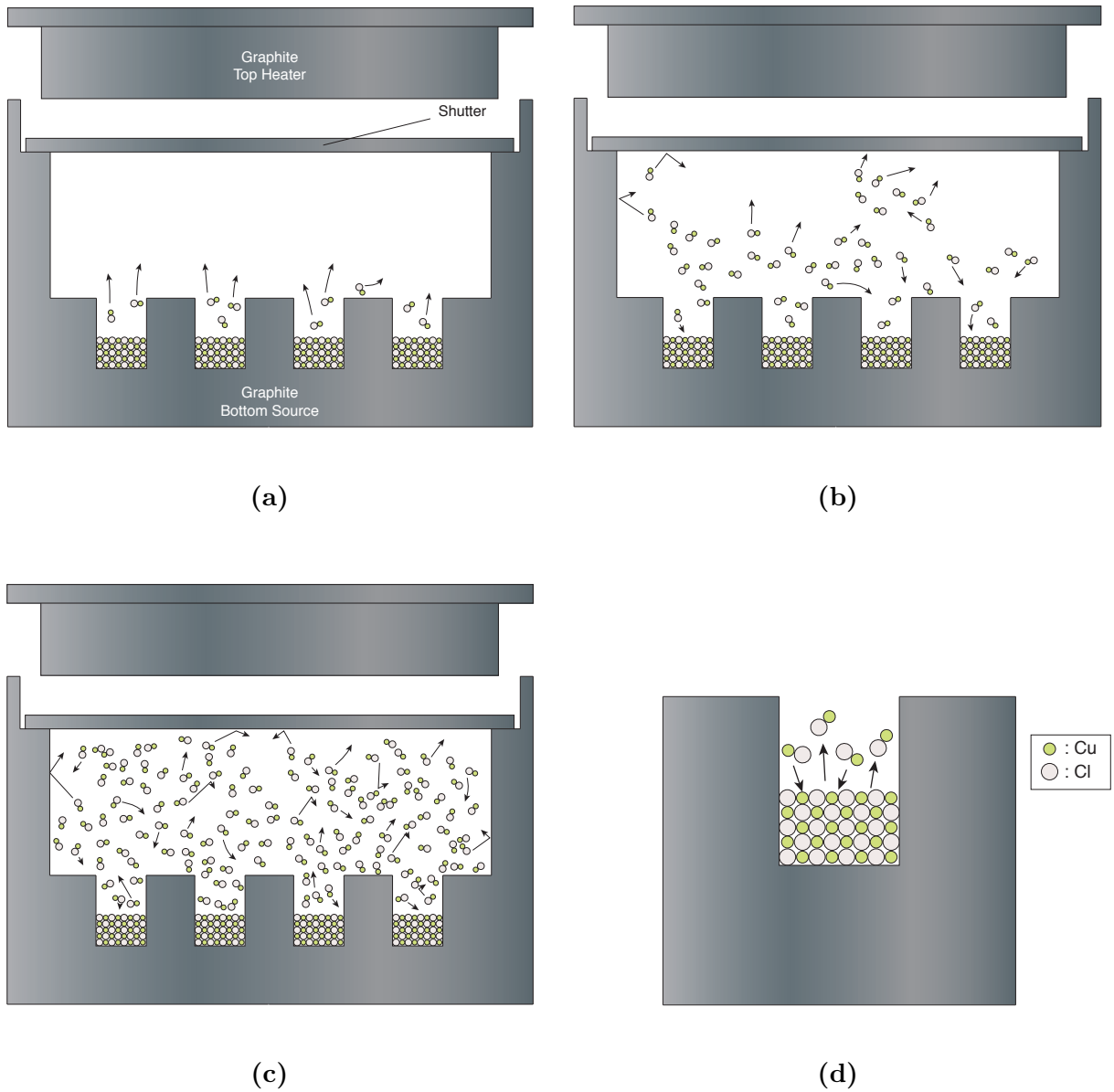


FIGURE 2.1. CuCl sublimation within the bottom source. CuCl partial pressure eventually reaches saturation as long as the surface temperatures within the pocket are equal and no leaks are present while the shutter is covering the source pocket. (d) is a zoomed representation of one of the bottom source wells from (c) when the evaporation rate is equal to the condensation rate at the solid-vapor interface.

equilibrium and thus sublimation is driven until the source sublimation rate, along with the deposition rate on the surface, again reaches equilibrium vapor pressure.

2.1.2. ADSORPTION. When the shutter is removed and the end-effector along with a substrate slides over the CuCl pocket, a thermal gradient is formed throughout the gaseous species (Figure 2.2). This is due to the substrate temperature $T_{substrate}$ being less than the temperature of the CuCl gas species monolayer directly adjacent to the substrate. The colder substrate surface acts as a thermal energy sink for these CuCl gas molecules, causing them to preferentially move toward it. As the CuCl vapor impinges on the surface, the gas molecule may lose enough kinetic energy during collision with the substrate in order to adhere to it, resulting in a process known as adsorption. Adsorption can either be a physical process that relies on Van Der Waals forces to hold the adsorbate gas species to the adsorbent bulk layer (a.k.a. physisorption) or a chemically activated process that combines both species with strong chemical bonds (a.k.a. chemisorption). The latter case creates a much stronger force and thus requires more energy to cause the gas molecule to desorb from the bulk layer. However, in this study physisorption is the dominant adsorption mechanism for CuCl on the FTO-coated substrate.

In order to fully understand how the adsorption rate is calculated, the rate of impingement by a gas on a particular surface must be determined. According to kinetic theory, the impingement rate is the amount of incoming molecules per second that hit a surface within a given area [18] and is expressed as follows:

$$(2.3) \quad \Phi = \frac{P}{\sqrt{2\pi MRT}}$$

where P = partial pressure of gas species impinging on the surface, M = gas species molar mass [kg/kg-mol], and T = temperature of the gas [K]. However, ANSYS® FLUENT tends to reformulate the impingement rate in terms of species concentration as oppose to

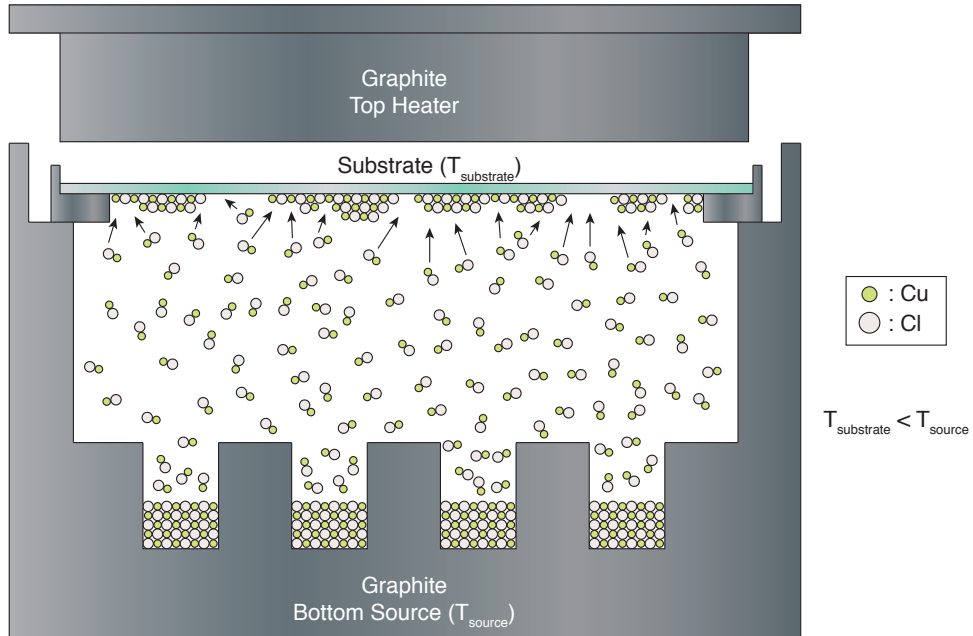


FIGURE 2.2. CuCl adsorption occurring at the substrate. Adsorption is dictated by a sticking coefficient on a given surface that can be attributed to one of the three systematic growth mechanisms.

partial pressure. Therefore equation 2.3 can be rewritten as:

$$(2.4) \quad \Phi = C_{\text{CuCl}_g} \sqrt{\frac{RT}{2\pi M}}$$

where C_{CuCl_g} is the CuCl molar concentration [kmol/m^3]. The impingement rate can be thought of as all incoming vapor molecules sticking to a surface. In reality, adsorption rates are typically much less than Φ due to imperfect surface conditions, preferred orientation, surface temperature, and ambient pressures. An overall representation of these complex limiting factors is known as the sticking coefficient S . This accommodating factor in its simplest form is written as:

$$(2.5) \quad S = \frac{R_{\text{adsorption}}}{\Phi}$$

As depicted in Figure 2.3, an impingement flux of CuCl gas occurs at some initial time t_0 , after which some Δt time passes, two possibilities are given: 1) all molecules impinging on the substrate stick to it ($S = 1$), or 2) some molecules do not stick and are reflected back into the vapor species ($S < 1$). In most real-world cases, S is a value between 0 and 1. Since the sticking coefficient is associated with many varying conditions of a given system, it is difficult to obtain a general solution for S that encompasses a wide range of systematic processes. Nonetheless, its contribution to the adsorption rate is a key aspect in thin-film growth analysis. Within this research work the sticking coefficient is attempted to be generalized for a certain CuCl temperature regime and process condition. Calculating S as a function of temperature may lead to a quantifiable model of the CuCl adsorption rate, but a brief look at the types of possible growth mechanisms in thin-films will help assess what type of growth behavior CuCl exhibits.

2.1.3. GROWTH MECHANISMS. Three growth mechanisms are used to classify the growth behaviors of thin-films according to the type of substrate and overlayer used during deposition: i) Volmer-Weber, ii) Frank-Van der Merwe, and iii) Stranski-Krastanov. Volmer-Weber growth occurs when clusters of the condensed species form islands on the substrate rather than a uniform layer. This is primarily due to the condensed species having a higher surface energy than the substrate to which it is adhering, making it more energetically favorable for island formation to occur. On the other hand, Frank-Van der Merwe is a layer-by-layer deposition phenomena in which the surface energy of the substrate is greater than the energy required to cluster the atoms together. The final mode known as Stranski-Krastanov growth is a combination of layered growth for the first few monolayers upon reaching a critical thickness where island growth becomes more favorable [18]. Previous studies have shown that the Stranski-Krastanov mode is prominent during CuCl heteroepitaxial growth on MgO

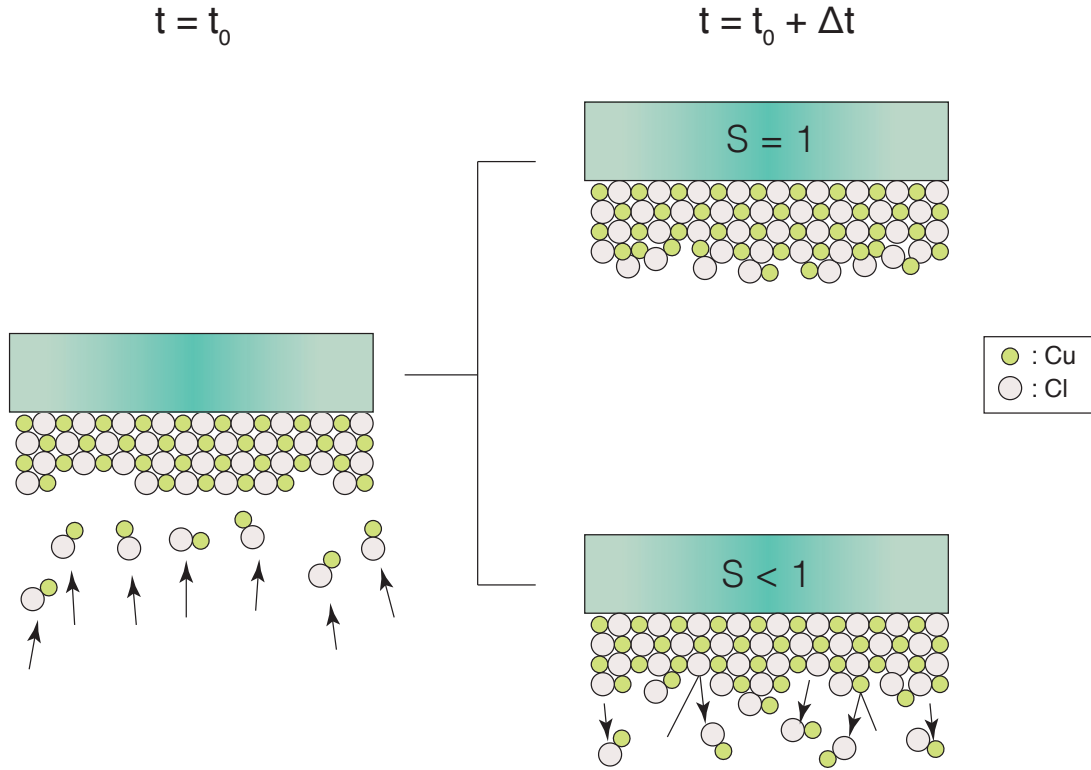


FIGURE 2.3. Schematic demonstrating the significance of the CuCl sticking coefficient

substrates [19, 20]. It was not known if CuCl would display similar growth characteristics within CSS as these studies, which is why the CuCl growth mechanism was investigated.

Figure 2.4 illustrates the growth modes in various thin-film structures.

2.2. SPECIES MODELING THEORY

ANSYS® FLUENT was the solver platform tool used for modeling the vaporization characteristics of CuCl during CSS. This engineering simulation program is geared toward computational fluid dynamics (CFD) as well as heat transfer/thermal modeling aspects. More specifically, FLUENT is capable of simulating finite-rate species transport and is most

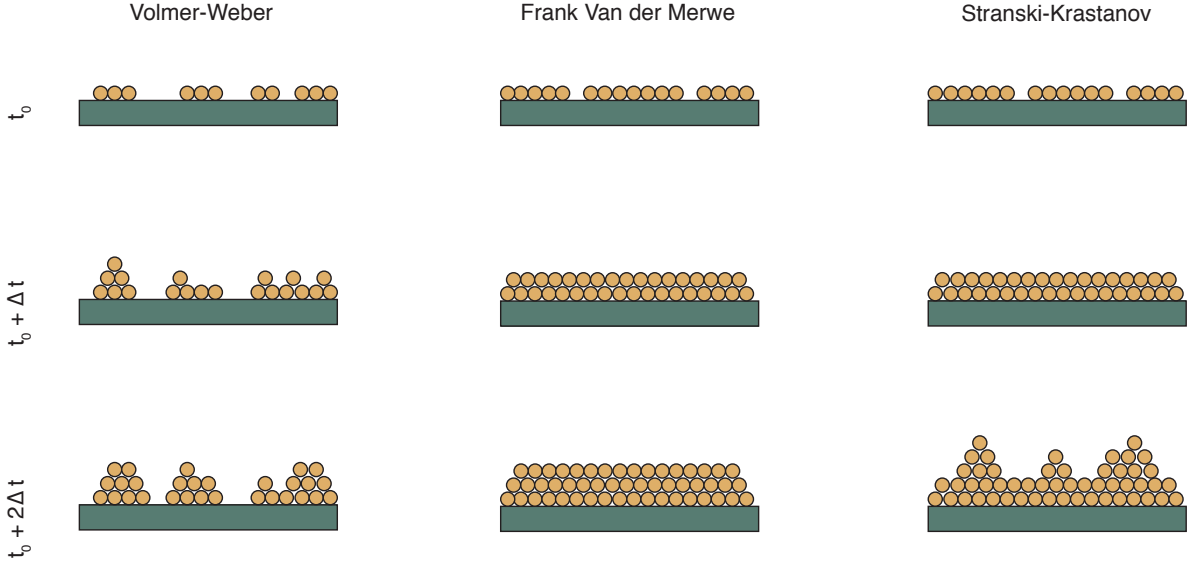


FIGURE 2.4. Primary growth modes displayed by various thin-films. Such modes are dependent on the surface energies of the substrate and adsorbed overlayer

applicable to this research work. For all simulations the species transport algorithm was enabled for describing the CuCl volumetric and wall-adhering species governed by the following equation:

$$(2.6) \quad \frac{\partial(\rho Y_i)}{\partial t} + \nabla \cdot (\rho \vec{u} Y_i) = -\nabla \cdot (\vec{J}_i) + R_i + S_i$$

where ρ = density, \vec{u} = momentum vector, Y_i = local mass fraction, \vec{J}_i = diffusion flux, R_i = net rate production, and S_i = source term of species i [21]. The first term on the left-hand side of the equation is the rate of change of the species mass fraction while the second term is related to convection. On the right-hand side, the first term is the divergence of the diffusion flux, the second term is the rate of production of the gas species i , and the third term an additional species source expression. Since the CuCl simulation was defined to be a steady-state problem with negligible convection effects and no additional source terms,

FLUENT only needs to calculate the diffusion flux \vec{J}_i as well as the net rate production of species i . An important flow characteristic that affects how the divergence terms are calculated is known as the Knudsen number (Kn). This dimensionless value classifies the flow regime of species within the volume geometry based off of their mean free paths. In other words, Kn determines whether molecules interact with each other more or less often than the dimensional limits of the chamber that surrounds them. The typical expression for Kn is in the form of a ratio:

$$(2.7) \quad Kn = \frac{\lambda}{L_c}$$

where λ is the mean free path of the gas molecule and L_c is the characteristic length of the chamber. At low $Kn < 0.1$, a continuous flow regime due to the high number of gas-to-gas collisions ensures the validity of the Navier-Stokes equations. On the other hand, high Kn values > 10 are seen in the molecular flow regime where bulk properties of diffusion are no longer relevant [22]. In between such limits is the transition flow regime where the no slip condition on the wall boundaries is invalid and should be accommodated by enabling the low-pressure boundary slip condition in FLUENT. For this particular simulation, negligible change in the deposition rate is seen using this condition. Furthermore, previous research on the CdS/CdTe domains in the main deposition chamber revealed that Kn was not high enough to affect the Navier-Stokes equations [6]. Thus it is assumed to cause minimal effects to the fidelity of the CuCl simulation. In the laminar flow case, the diffusion flux can be described by:

$$(2.8) \quad \vec{J}_i = -\rho D_{i,m} \nabla Y_i - D_{T,i} \frac{\nabla T}{T}$$

where $D_{i,m}$ = mass diffusion coefficient and $D_{T,i}$ = thermal diffusion coefficient for species i . It is evident from equation 2.8 that the diffusion flux is dictated by both the concentration and thermal gradient across the CuCl vapor species and will consequently determine the deposition rate possible on a specified wall surface. Both the mass and thermal diffusion coefficients $D_{i,m}$ and $D_{T,i}$ were calculated using the available kinetic theory option under mixture materials. Two inputs known as the Lennard-Jones (L-J) parameters were necessary for solving any material properties governed by kinetic theory. The L-J characteristic length σ is described as the equilibrium distance between two given atoms during which zero net energy (i.e. repulsive energy - attractive energy = 0) is acting on them. The energy parameter ϵ/k_b is attributed to the minimum potential energy well (i.e. highest attractive energy) between two atoms that induce dipole moments in each other [23]. There are no readily available L-J parameters for CuCl within research literature, thus a simple calculation using data obtained from Monte Carlo simulations on Cu [24] and Cl [25] was performed via the Berthelot Mixing Rule:

$$(2.9) \quad \sigma_{ab} = \frac{\sigma_{aa} + \sigma_{bb}}{2}$$

$$(2.10) \quad \epsilon_{ab} = \sqrt{\epsilon_{aa}\epsilon_{bb}}$$

where a and b refer to Cu and Cl, respectively. The calculated parameters for CuCl were $\sigma = 2.789 \text{ \AA}$ and $\epsilon = 914.087 \text{ K}$.

The Pressure-Based Coupled Solver used in this simulation initially solves for the mass and momentum equations, which is followed by the energy equation for each iteration. Such equations will compute the main domain properties such as temperature, density, enthalpy, velocity components, and pressure at each cell-center of the mesh. Thereafter equation 2.6

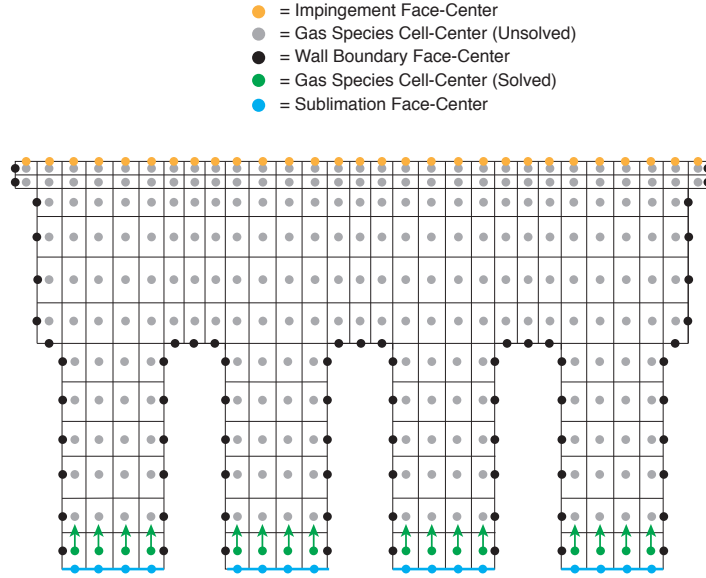
is calculated along with the aforementioned properties per iteration until their residuals converge to a steady-state condition. The final solution provides Y_i cell-center values necessary to describe the CuCl concentration gradient throughout the pocket (Figures 2.5a and 2.5b). The wall surface conversion process represented as CuCl species in the model is defined as:

$$(2.11) \quad b_1' \cdot CuCl_b + s_1' \cdot CuCl_s = s_1'' \cdot CuCl_s + g_1'' \cdot CuCl_g$$

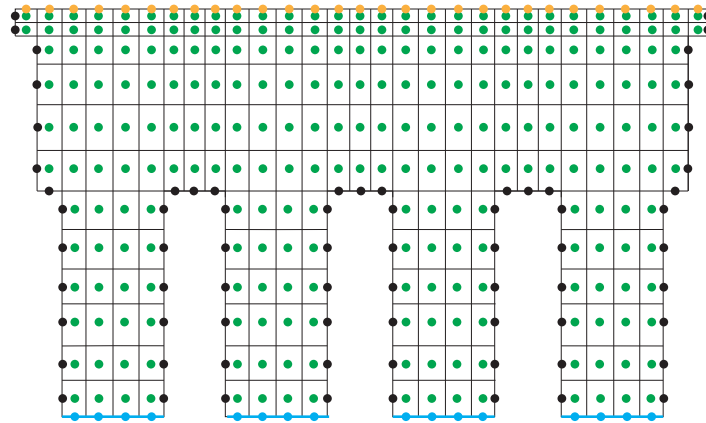
$$(2.12) \quad g_2' \cdot CuCl_g + s_2' \cdot CuCl_s = s_2'' \cdot CuCl_s + b_2'' \cdot CuCl_b$$

where the g , s , and b subscripts respectively denote gas, site, and bulk species of CuCl. b_1' , s_1' , g_2' , and s_2' are the initial species stoichiometric coefficients while s_1'' , g_1'' , s_2'' , and b_2'' are the final species stoichiometric coefficients of the kinetic processes. The subscripts 1 and 2 denote sublimation and impingement, respectively, and all stoichiometric coefficients are equal to 1. Since $CuCl_g$ is assumed to be a non-dissociative molecule during the entire simulation process, the equations are straightforward for converting species in both kinetic processes. Equation 2.11 states that the CuCl bulk species in combination with an available CuCl site will desorb from a wall surface in the form of a CuCl gas molecule at some rate constant k_r . Similarly, equation 2.12 describes the wall surface kinetic rate for impingement, during which the gas species $CuCl_g$ cell-center values directly adjacent to the substrate wall are converted into the $CuCl_b$ bulk species values that are representative of the impingement rate on the substrate (Figure 2.6). FLUENT interprets the process rate constants using the following Arrhenius expression:

$$(2.13) \quad k_r = A_r \cdot T^\beta \cdot \exp\left(\frac{-E}{RT}\right)$$



(a)



(b)

FIGURE 2.5. Schematic of species transport calculation throughout entire mesh domain. (a) Sublimation kinetic rate is enabled to allow FLUENT to compute and store the mass fraction Y for CuCl in the cell-centers that are compared to surrounding values that determine whether a solution for $\nabla \vec{J}_i = R_i$ has converged. (c) After convergence, the 1st adjacent cell-center layer to the substrate impingement face-centers will influence the impingement rate calculated to obtain a simulated CuCl thickness.

It should be evident that equation 2.13 is a modified form of equation 2.2 with an additional temperature term raised to some β constant. Furthermore, the k_r rate constant can be simplified to match the form of impingement rate equation 2.4. Setting $r = 1$ for

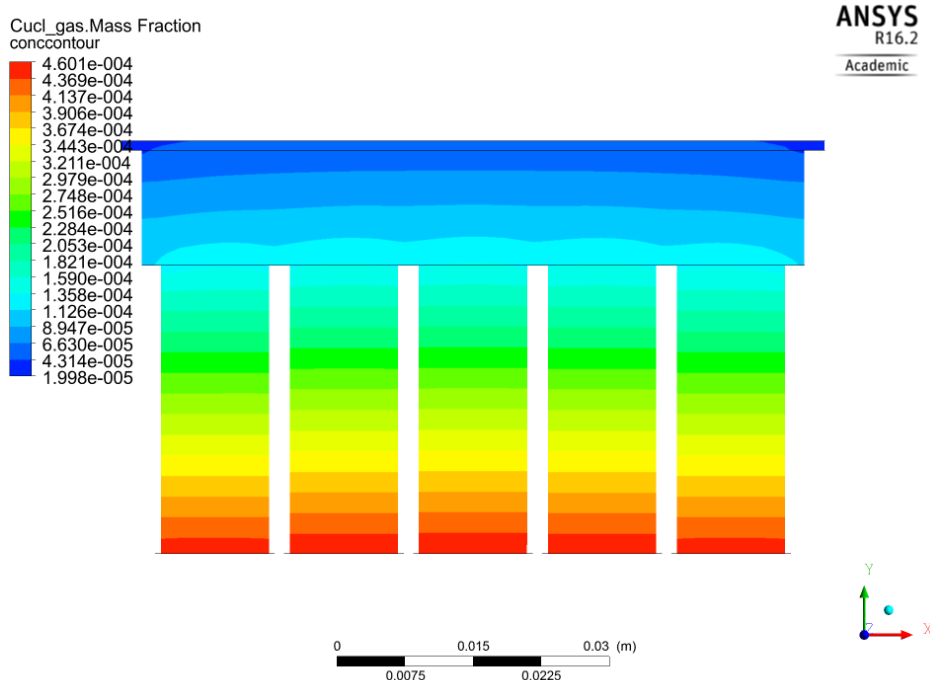


FIGURE 2.6. Example of CuCl mass fraction calculated in simulation model based off of R_1 (sublimation) at the bottom source and R_2 (impingement) at the substrate

sublimation and $r = 2$ for impingement, the final kinetic rates R_1 and R_2 may be expressed as follows:

$$(2.14) \quad R_1 = -A_1 \cdot \exp\left(\frac{-E}{RT_{source}}\right) + B_1 \cdot C_{CuCl_g} - C_1$$

$$(2.15) \quad R_2 = A_2 \cdot C_{CuCl_g} \sqrt{T_{substrate}}$$

where A_1 and A_2 can be derived from calculating the constant terms in equations 2.2 and 2.4 respectively. B_1 and C_1 were included in equation 2.2 to provide additional functionality to the sublimation rate with respect to CuCl partial pressure if necessary. By activating these kinetic mechanisms on particular wall surfaces as well as applying the stoichiometric coefficients from equations 2.11 and 2.12, a net molar rate of production or consumption [kg-mol/m²-s] on a particular wall of the mesh domain can be calculated to determine the

gas, site, and bulk CuCl species. Equations 2.16 - 2.18 define these calculations for each respective term:

$$(2.16) \quad \hat{R}_g = (g_1'' - g_1') \cdot R_1$$

$$(2.17) \quad \hat{R}_s = 0$$

$$(2.18) \quad \hat{R}_b = (b_2'' - b_2') \cdot R_2$$

where g_1'' and $b_1'' = 1$ and g_1' and $b_1' = 0$. It should be noted that $R_s = 0$ means that the CuCl site species is constant throughout the entire wall surface adsorption process. A reaction-diffusion balance is made at the wall during each iteration until steady-state convergence is achieved, during which the mass deposition rate on the wall surface is calculated:

$$(2.19) \quad \dot{m}_{dep} = M \cdot \hat{R}_b$$

Again, $M = \text{CuCl molar mass [kg/kg-mol]}$. Converting the units of \dot{m}_{dep} from [kg/m²-s] to [nm/s] will ultimately lead to the simulated impingement rate Φ as shown by equation 2.20:

$$(2.20) \quad \Phi = \frac{\dot{m}_{dep} \cdot 10^9}{\rho}$$

Multiplying the impingement rate Φ by the deposition time t provided a simulation thickness at each particular substrate and source temperature for further comparison to experimental thicknesses, which will be described in the next chapter.

CHAPTER 3

EXPERIMENTAL/SIMULATION METHODS

The experiments performed within this research were focused on quantifying both the sublimation and adsorption rates of CuCl during the CSS process. Since the simulation of CuCl thin-film growth rates required an accurate representation of sublimation within the CSS apparatus, CuCl mass-loss measurements were recorded and used for further sublimation rate calculations. This chapter will explain the method of measuring the CuCl sublimation rate and the obtained Arrhenius rate expression used within ANSYS® FLUENT. It will also elaborate on the multi-step technique developed to measure the CuCl thickness across the substrate at pre-determined locations. Finally a description of the mesh model, along with its boundary conditions obtained from theoretical aspects defined in Chapter 2, will be elaborated for CuCl thickness simulations. This chapter aims to bridge the gap between CuCl experimental and simulated growth rate results.

3.1. CSS TECHNIQUE IN CuCl THIN-FILM GROWTH

CuCl growth rates were varied by sweeping a range of thermal parameters for each deposition run using the Advanced Research Deposition System (ARDS). This versatile tool contains several CSS stations, each equipped with a graphite top heater and bottom heating source where the material powder, in this case CuCl, is sublimated. Both the top heater and bottom source temperatures are adjusted by electrically heating the Nickel-Chromium coil embedded in each graphite fixture and maintained via PID control. The heaters were kept at near steady-state conditions since temperature fluctuations (top heater: 1-2°C, bottom source: < 1°C) occurred due to the PID control setup. Approximately 63.9 SCCM of mixed gas (98% N₂, 2% O₂) is flown throughout the chamber while maintaining an ambient pressure

of 40 mTorr using a Leybold D65 rotary vane mechanical pump and a Varian VHS-4 diffusion pump.

Pilkington TEC-12D glass substrates (78 x 90 mm²) were used during each deposition run and were ordered with a TCO pre-layer consisting of FTO covering one side of the glass. The substrates were initially rinsed, sonicated, and N₂ dried [11] to keep surface conditions as clean as possible. All substrates were plasma-cleaned in a 200 mTorr N₂ environment for 30 s before entering the main chamber. Initial CuCl experiments were performed at normal process of recipe (POR) conditions, which pertain to heating the substrate to > 400°C prior to thin-film deposition and depositing CuCl on the substrate for 110 s. However, thicknesses of the resulting CuCl thin-films were too inconsistent to be measured with any available instruments. Therefore, it was decided that all substrates were to directly enter the CuCl domain without pre-heating and deposit for one hour to obtain easily measurable CuCl thin-films as well as reach steady-state equilibrium conditions within the domain. As a result, CuCl films were produced with a thickness that could be measured consistently and accurately.

Two sets of experiments were ran in the ARDS: 1) full-well and 2) single-well deposition. Full-well deposition refers to all 20 wells in the graphite bottom source being 1/2 filled with CuCl powder, which is the typical POR setup for all sublimation sources. As the name implies, single-well deposition only used one well 1/2 filled with CuCl while leaving the other 19 source wells empty. Simulation models for both cases were also developed and compared to the experiments. The full-well deposition case was used to check the initial accuracy of the impingement rate obtained from the simulation and compare it to the actual adsorption rate given by experimental data. A sticking coefficient curve fit for each substrate and source temperature could then be obtained for later use with the single-well deposition model. The

full-well runs were also used to determine the growth mode exhibited by CuCl on the FTO layer via characterization analysis. The main goal for using the single-well deposition case was to verify the model's accuracy in describing the physical processes associated with CSS during an extreme processing condition. Actual images of the full and single-well CuCl setups can be found in Figures 3.1a and 3.1b.

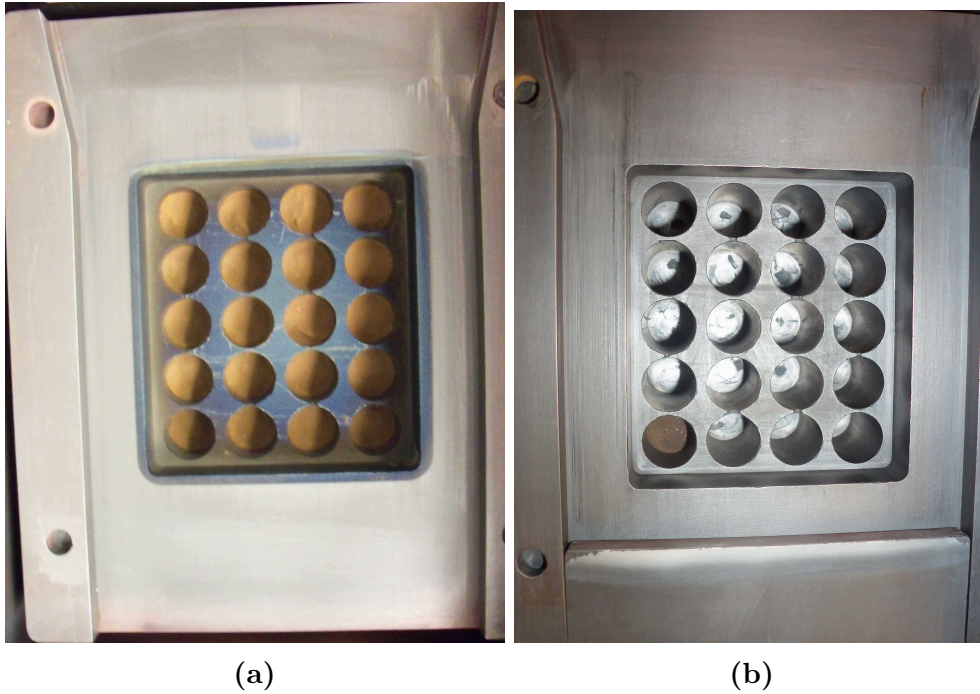


FIGURE 3.1. (a) Full-well and (b) single-well depositions in the ARDS. Upon further analysis, the distinct color difference between experiments indicated whether the CuCl powder continuously sublimated (darker) or not (lighter) after completing all deposition runs.

Top heater and bottom source temperatures were systematically varied per substrate. It was necessary to determine the substrate temperature during each deposition run. However the Mikron-MI-N5/5+ series pyrometer installed at the CuCl chamber entry was unable to properly measure the substrate temperatures, either due to calibration error in emissivity, pyrometer positioning, or a combination of both. It was decided that substrate temperatures were to be calculated using a simplified radiation heat transfer expression dependent on the

top and bottom CuCl coil temperatures. The net radiation between two surfaces [26] is found by:

$$(3.1) \quad q_{12} = \frac{\sigma(T_1^4 - T_2^4)}{\frac{1-\epsilon_1}{\epsilon_1 A_1} + \frac{1}{A_1 F_{12}} + \frac{1-\epsilon_2}{\epsilon_2 A_2}}$$

where σ = Stefan-Boltzmann constant [5.67×10^{-8} W/m²·K⁴], F_{12} = view factor, ϵ_1 , ϵ_2 = emissivity, A_1 , A_2 = surface area, and T_1 , T_2 = surface temperatures for surface 1 and 2, respectively. The following assumptions were made during the substrate temperature calculation:

- (1) Substrate glass emissivity is constant on the top surface ($\epsilon_{s,t} = 0.8$)
- (2) TCO emissivity on the bottom of the substrate is constant ($\epsilon_{s,b} = 0.2$)
- (3) Top heater, bottom source, and substrate surfaces considered to be parallel long plates since they are all in close enough proximity to each other
- (4) All surfaces are isothermal
- (5) Steady-state conditions have been reached

Such assumptions were reasonable considering the graphite heaters were uniform in temperature ($\pm 1^\circ\text{C}$) and the deposition time (1 hr) was longer than necessary to reach steady-state thermal conditions in the CuCl domain. Figure 3.2 illustrates the concept of the substrate temperature calculation. Using these assumptions and solving the energy balance by equaling the radiation heat transfer rates between the bottom source to the substrate ($q_{\text{bottom-substrate}}$) and substrate to the top heater ($q_{\text{substrate-top}}$), the substrate temperature was expressed as:

$$(3.2) \quad T_{\text{substrate}} = (0.222 \cdot T_{\text{CuCl,bottom}}^4 + 0.778 \cdot T_{\text{CuCl,top}}^4)^{1/4}$$

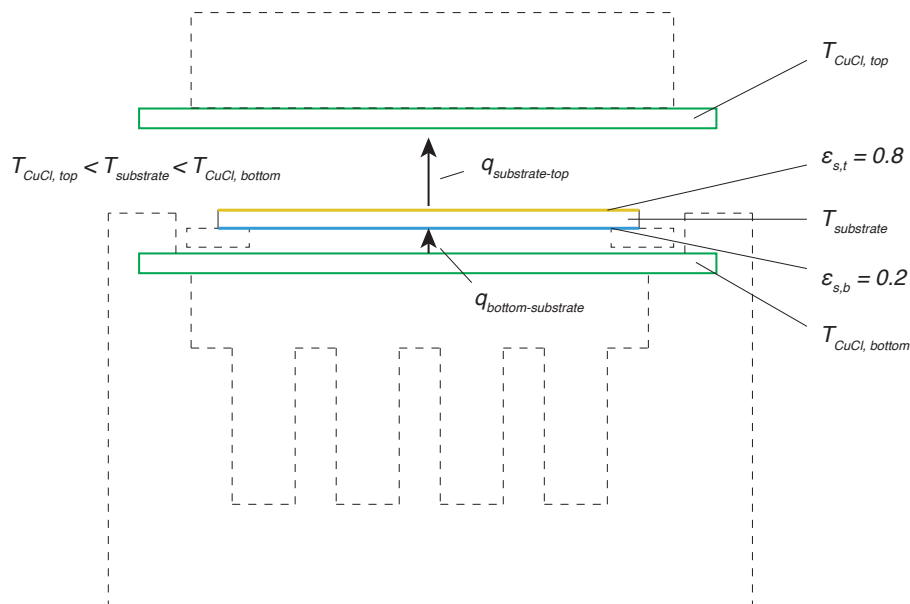


FIGURE 3.2. Illustration of the substrate temperature calculation

where $T_{CuCl, bottom}$ and $T_{CuCl, top}$ were the respective bottom and top CuCl heater temperatures. All substrate depositions (full and single-well) were classified by their substrate and source temperatures as recorded in Tables 4.1 and 4.4 found in Chapter 4.

3.2. CuCl MASS-LOSS EXPERIMENT

Studies on CuCl vapor pressure [7, 27–29] during sublimation were analyzed to see if their vapor pressure curves embodied the standard kinetic rates found in the ARDS operation regime. However, CuCl sublimation rates at temperatures $< 300^{\circ}\text{C}$ were not well defined in previous literature and most studies performed experiments at different baseline pressures than the typical ARDS operating pressure (40 mTorr). Larger molecular vapor species such as Cu_3Cl_3 trimers are more prevalent at higher temperatures than the expected CuCl vapor [7], further deviating from CSS conditions. It was not known if such sublimation rates were representative of that seen in CSS and was therefore imperative to obtain an empirical expression for the CuCl sublimation rate within the ARDS. This would ensure the data

used to calculate the sublimation rate were within the applicable temperature and pressure regimes and could be applied to the simulation model.

The CuCl mass-loss experiment was performed in the ARDS CuCl bottom source using four graphite crucibles machined to fit in the source wells. Each crucible was weighed five times before and after sublimating using a Mettler AE163 mass balance. The crucibles were filled with 1/4 tsp of CuCl powder and baked for approximately 18 hours to minimize the amount of water vapor accumulation in the materials and replicate typical CuCl powder conditions after an extended period of usage. The crucibles were sublimated at 210, 220, and 230°C for 18 hours at each temperature to ensure steady-state sublimation. Previous experiments revealed prolonged exposure to ambient conditions noticeably affected mass measurements. It is believed that water vapor was the main culprit to this detrimental factor. Each experiment run was performed immediately after measuring CuCl mass to prevent the crucibles and/or CuCl powder from collecting water vapor and resulting in misleading mass analyses. Temperature logs were recorded for the bottom source within the CuCl domain to determine whether thermal equilibrium was sustained throughout the entire sublimation process (Figure 3.3). After calculating the CuCl mass-loss at each particular source temperature and crucible, a log curve fit was applied to the entire data set to define the sublimation rate as an Antoine expression shown in equation 2.1:

$$(3.3) \quad \log(R_{sublimation}) = \frac{-6503.8}{T} + 4.8741$$

The Arrhenius rate expression derived from equation 3.3 is provided:

$$(3.4) \quad R_{sublimation} = 74831.93 \cdot \exp\left(\frac{-1.2451e8}{RT}\right) [kg\text{-mol}/m^2 \cdot s]$$

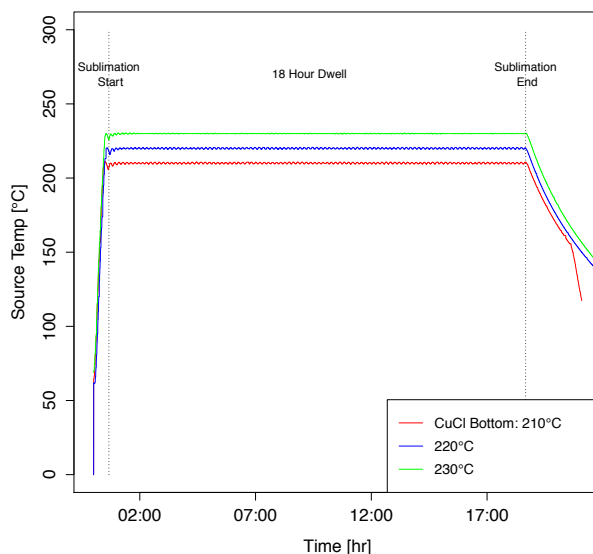


FIGURE 3.3. Temperature plot of the 18-hr sublimation experiments ran at CuCl bottom source temperature = 210, 220, and 230°C

As previously mentioned in Chapter 2, the temperature-dependent Arrhenius rate expression was applied to the simulation model as the driving mechanism for sublimation in the CuCl source pocket. This would allow for the CuCl concentration to be calculated throughout the CuCl pocket domain and influence the impingement rate on the substrate. The fulfillment of the CuCl mass-loss experiment provided empirical data for the CuCl sublimation rate within the CSS system operating at 40 mTorr and was implemented in the CuCl growth simulation model for further thin-film growth analysis.

3.3. CuCl THICKNESS MEASUREMENT TECHNIQUE

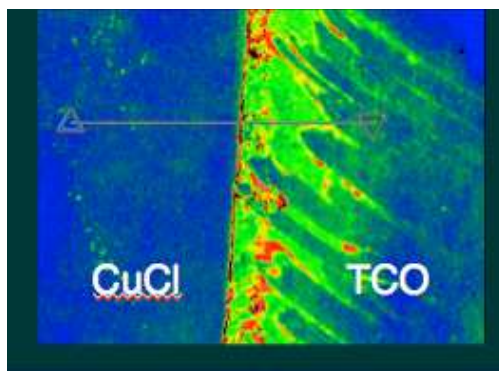
3.3.1. FORMER METHODS. A consistent method needed to be developed in order to compare experimental growth processes to simulated behaviors. However, many challenges were encountered in measuring CuCl thin-film thickness due to short deposition times and measurement techniques. In previous research of Cadmium Sulfide deposition within the ARDS [6], the primary method of measuring the thin-film thickness was to mask one side

of the diagonal of the substrate with etchant tape and etch away the unmasked side with Hydrochloric Acid (HCl). Doing so created a step height between the now bare TCO layer and the CdS overlayer that was measured across the entire substrate diagonal. Similar attempts were made to measure the CuCl thicknesses using this method while depositing CuCl near POR conditions (110 s). But since CuCl was much thinner than CdS at POR, etching one side of the CuCl layer would unexpectedly roughen the TCO below and lead to misleading thickness results.

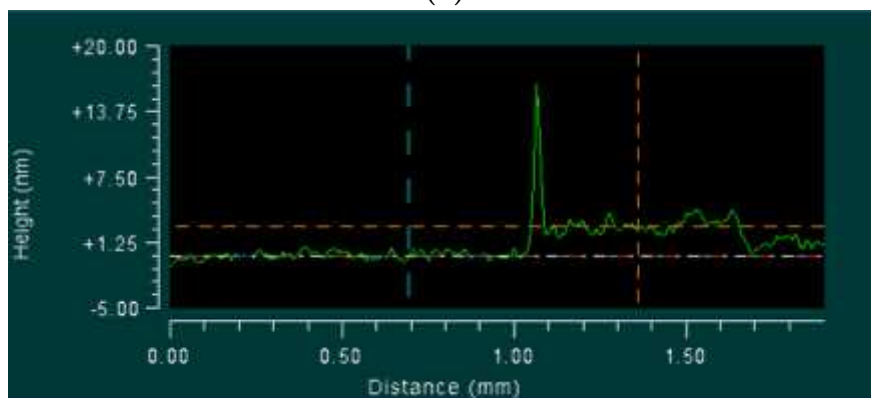
The next attempt included dripping one or a combination of the three solutions, Isopropanol (IPA), de-ionized water (DI), or Acetone, on the CuCl layer to create craters as the measured step heights. CuCl deposition was again done for 110 seconds. Unfortunately the craters formed by either solution migrated CuCl to their outer perimeters and caused erroneous delta steps that were not representative of the thickness as shown in Figures 3.4a and 3.4b. The same effect occurred when substrates were dipped in either IPA or DI. Furthermore, the 110 s CuCl depositions had very little CuCl on the substrates (< 5 nm), making measurements unfeasible with the available instruments.

3.3.2. CURRENT METHOD. A new multi-step method was implemented to measure the CuCl thicknesses accurately and consistently. The method is summarized into three subsequent steps: 1) Argon Ion Beam sputtering to form a crater deep enough into both the CuCl and TCO layers, 2) measuring the crater depth using scanning white light interferometry (SWLI), and 3) etching CuCl overlayer with HCl and remeasuring the crater depth to determine the overall step height difference.

3.3.2.1. Argon Ion Beam Sputtering. The Argon Ion Beam in the X-ray Photoelectron Spectroscopy (XPS) instrument was utilized to create 10 craters shaped like a rounded rectangle across the diagonal of each substrate. Micrometer dial positions were determined



(a)



(b)

FIGURE 3.4. (a) Contour representation and (b) thickness profile plot of CuCl after DI and Acetone was dripped on substrate. Generalizations of CuCl thin-film growth with respect to temperature could not be made using this inconsistent method, thus a new technique was devised for measuring CuCl thicknesses.

for each particular crater location to ensure coordinate consistency (Figures 3.5a, 3.5b). As shown in Figure 3.6, the Ion Gun propelled ionized Ar atoms toward the substrate with an accelerating voltage of 5 kV, using kinetic energy to collide with the exposed surface atoms and remove them. Over time a crater would develop within both the CuCl and TCO layer below so that a thickness step height could later be measured. Typical operating pressures within the XPS were $9 \times 10^{-8} - 2 \times 10^{-7}$ Torr over the duration of the Ar^+ sputtering process. Each process was timed for 5 minutes to form a crater deep enough in the CuCl and TCO layers¹.

¹See Appendix A for details on XPS of CuCl/TCO crater before and after Ar^+ sputtering

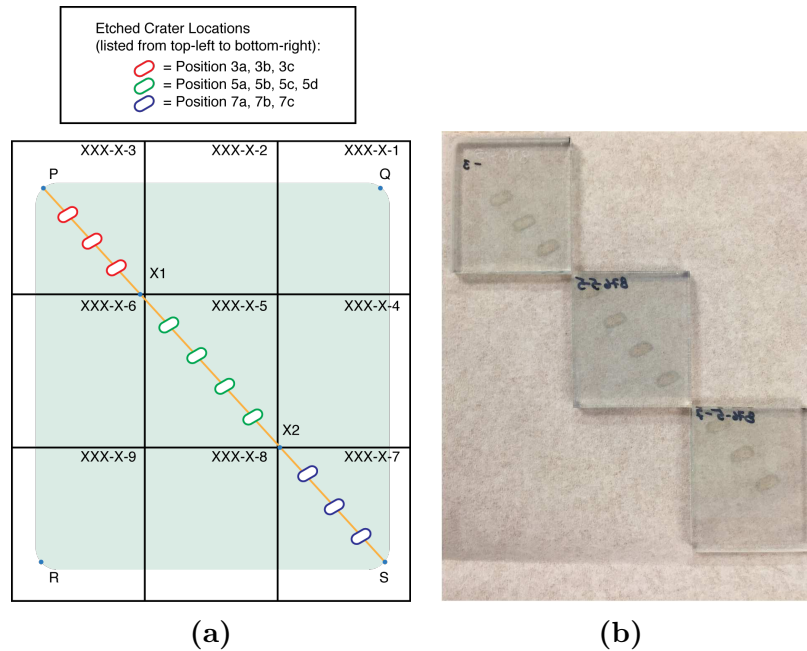


FIGURE 3.5. (a) Expected CuCl crater locations and (b) typical crater locations on a TEC-12D substrate. The substrate is divided into 3 x 3 samples that are labeled by position values 1-9. Only positions 3, 5, and 7 are used for crater etching

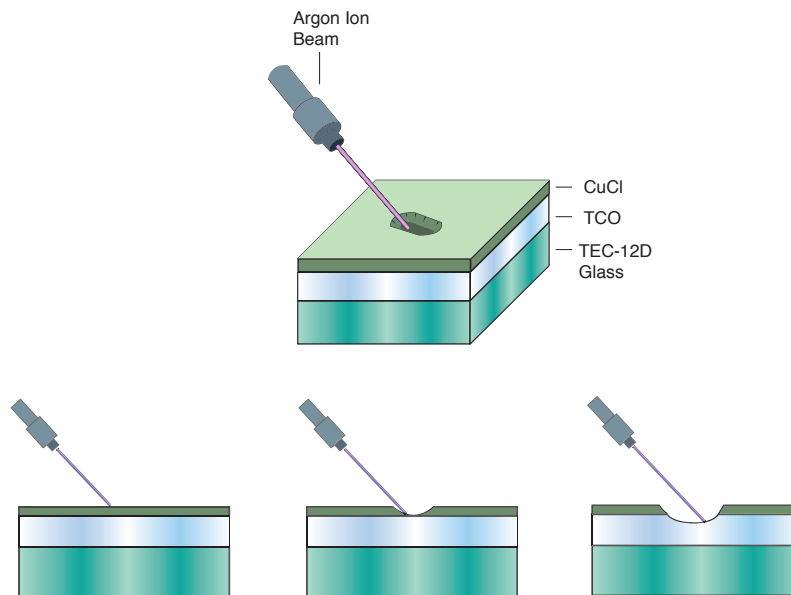


FIGURE 3.6. Schematic of CuCl/TCO crater formation during Ar^+ sputtering process

3.3.2.2. *Scanning White Light Interferometry.* The NewView 7300 instrument used for measuring the CuCl thicknesses is known as a Scanning White Light Interferometer (SWLI). This tool implements a nondestructive technique known as Coherence Scanning Interferometry [30] that evaluates the metrology of a sample using a broadband spectrum (white light) traveling toward the surface and reflects off of it, producing interference fringes at a certain scan height. The instrument vertically scans the entire topology along its optical axis, obtaining contrast fringes throughout the entire scanning process. Frames at each height variation are acquired successively by a 640×480 pixel CCD camera and processed into an areal (3-D) representation of the surface (Figure 3.7a). For each small sample (26 x 30 mm²) SWLI measured the crater depth before etching the CuCl thin-film with HCl. After the first measurement, the CuCl layer was removed with HCl and cleaned with DI and IPA to eliminate etchant residue and marks. A second measurement was performed on the etched samples to determine the remaining TCO crater depth. The difference between the first and second depth measurements resulted in a CuCl thickness at the crater location.

For all measurements, a gaussian spline low-pass filter with a filter high wavelength of 0.08 mm was included to reduce the surface noise due to CuCl roughness (3-5 nm) and establish a CuCl thickness measurement closer to the average step height difference. The instrument scanning distance was set at 40 μm to capture the entire topology on the substrate surface. As shown in Figure 3.7b, a reference and test mask were created as the crater depth displacement planes and all measurements were recorded using the evaluated peak-to-valley mean values. For the reference mask areas (longer rectangular areas), a best fit cylinder form was applied to remove the curvature within each sample due to thermal warping while in the ARDS chamber. As a result, the mean top plane was analyzed in place of the curved surface plane. Within the test mask (large square area) a high clipping parameter was specified to

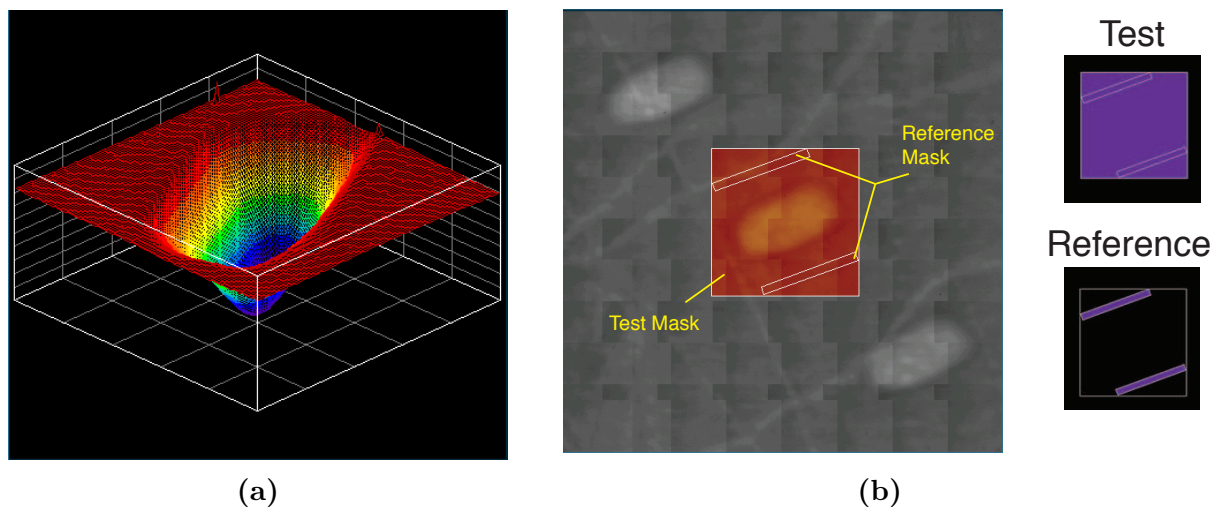


FIGURE 3.7. (a) Areal representation of a typical CuCl crater measured with SWLI. (b) Test and reference mask used within CuCl crater depth analysis, where the test mask is the entire area shaded in orange (purple) and the reference masks are the long rectangular boxes used as leveling planes for each data set.

remove any data > 2 nm above the deepest part of the crater. The average of the remaining several thousand data points within the deepest crater area was used to measure the mean CuCl step height to the top reference plane. The measurement process at each crater location was repeated across the substrate diagonal and compared to the CuCl thickness simulation results.

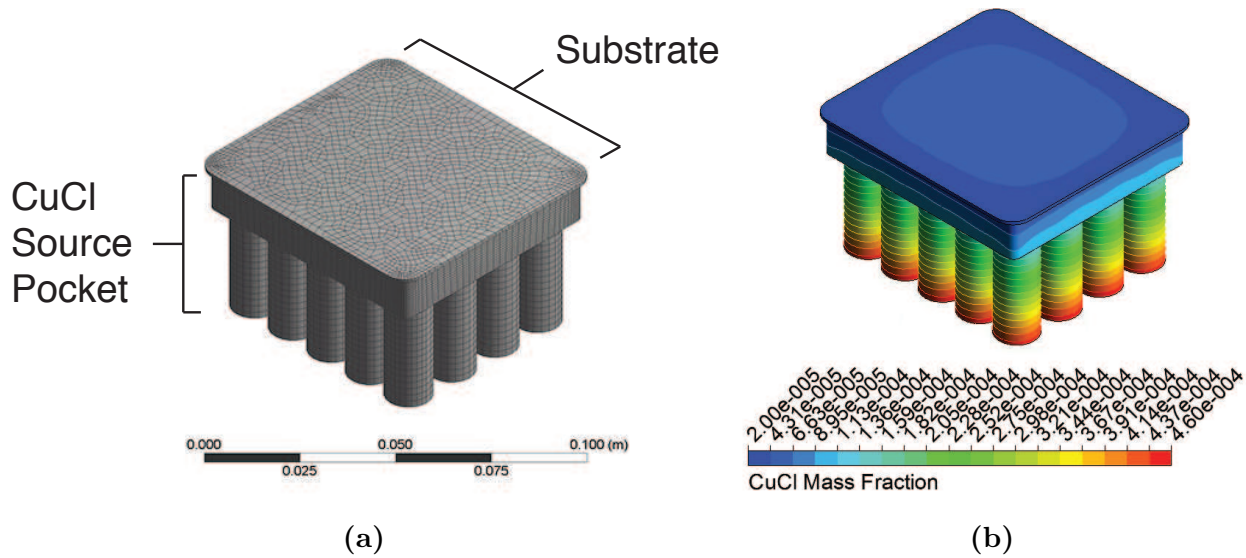
3.4. SIMULATION METHOD

The CuCl thin-film growth simulation model required an extensive study on material properties of CuCl from various literature sources [31–35] as well as experimental data obtained from this study. A CuCl materials database, along with any materials used within the ARDS, were compiled in order to properly develop the thermal and diffusional characteristics of CuCl amidst a N_2 - O_2 bulk gas in the pocket mesh. As shown in Figure 3.8a and 3.8b, the 3D CuCl mesh model used during the CuCl growth rate simulation consisted of 45772 nodes with a minimum orthogonal quality of 0.49 and maximum skewness of 0.74.

These mesh property values were considered to be adequate for computationally accurate simulations of CSS. Only steady-state simulation analyses were conducted in this research study since the one hour deposition time used in the experiments was assumed to achieve steady-state thermal and kinetic conditions within the ARDS. Furthermore, using transient analysis did not improve the modeling accuracy and thus only extended the computational time necessary to reach convergence.

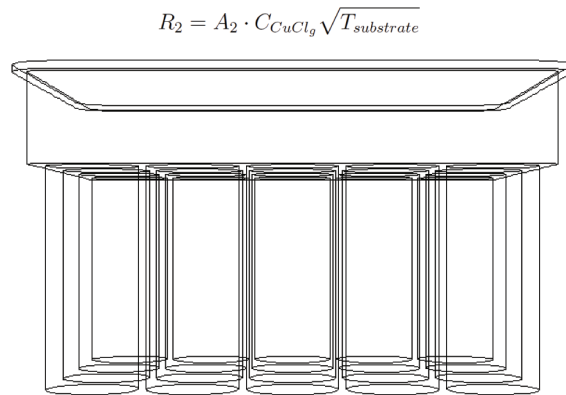
Certain mesh boundaries were specified as primary sublimation or impingement surfaces. The largest volume of the mesh geometry represented the CuCl bottom source pocket where the cylindrical wells contained the CuCl powder to be sublimated into a vapor species. The top mesh region composed of the smaller volume region encased by the end effector walls and the substrate surface adjacent to the pocket domain. Depending on whether a full-well or single-well simulation was performed, the bottom well sources were marked as walls separate from the other pocket geometry boundaries and assigned as sublimation sources defined by equation 3.4. The substrate face was classified as the impinged region with a rate described by equation 2.4 (Figure 3.8c). The inputs for each simulated case were the source and substrate temperature along with their respective kinetic mechanism (see Section 2.2 for more information on the species modeling theory). The entire bottom source wall boundaries were kept at a uniform temperature since thermocouple data showed only a $\pm 1^\circ\text{C}$ difference between the bottom source side walls (see Appendix B for more information).

CuCl sublimation and impingement was enabled after initializing and converging the initial state inputs with regards to temperature on each wall (1000 iterations). Each simulation was ran until the residuals reached suitable convergence (approximately 3000 iterations per case). Using 150 points plotted across the substrate wall diagonal (Figure 3.9), the CuCl deposition rate was obtained at each point. The data was exported with columns of the



(a)

(b)



$$R_1 = -A_1 \cdot \exp\left(\frac{-E}{RT_{source}}\right) + B_1 \cdot C_{CuCl_9} - C_1$$

(c)

FIGURE 3.8. CuCl (a) mesh model used during FLUENT simulation, and (b) contour example when kinetic rates were activated to determine the CuCl mass fraction throughout the pocket. This example was performed at a substrate and source temperature of 180.6°C and 210°C, respectively. (c) Specified kinetic rates R_1 and R_2 at the bottom well source and top substrate wall boundaries, respectively.

deposition rate [nm/s] and location along the substrate diagonal [mm]. All deposition rates were multiplied by $t = 3600$ s to determine what the predicted thickness would be after one hour deposition and were compared to experimental results according to substrate and source temperature parameters.

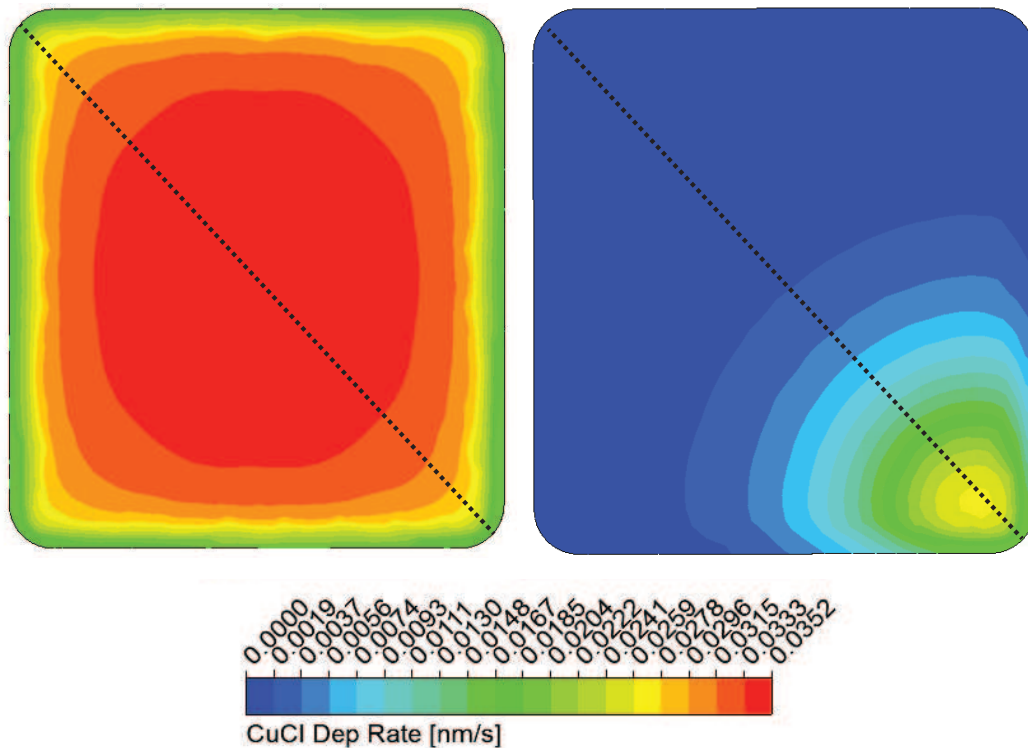


FIGURE 3.9. Examples of full well and single well simulation deposition rates. Along the black dotted line are where 150 points were mapped across the substrate diagonal to measure the deposition rate profile from position 3 to 7 (referenced by Figure 3.5a) on the substrate for comparison to experimental results. These two examples were modeled at a substrate and source temperature of 191.7°C and 210°C, respectively.

CHAPTER 4

RESULTS/DISCUSSION

CuCl thicknesses were obtained for full-well CSS depositions as a function of substrate and source temperatures. Sticking coefficient values were calculated and plotted to develop curve fitting parameters that would improve the initial accuracy of the full-well simulation models. The converged model along with sticking coefficient curves for a given source temperature was later applied to single-well depositions to verify its computational accuracy at such a vastly different process condition. In order to gain a further understanding of the inherent growth mechanisms exhibited by CuCl during CSS process conditions, characterization via Scanning Electron Microscopy (SEM) and Electron Dispersion Spectroscopy (EDS) were performed on the full-well experiments. This chapter aims to provide the aforementioned results while elaborating on their significance to CuCl thin-film deposition and growth analysis. A discussion on the various implications within the data will be made, which will be used to draw conclusions on the proposed CuCl growth mode as well as current modeling accuracy in representing the CuCl vaporization process and the resulting thin-film uniformity during CSS.

4.1. FULL-WELL DEPOSITION

As mentioned in Section 3.1, TEC-12D substrates initially entered the ARDS chamber without prior heating, during which CuCl was deposited for one hour. Substrates with a lower surface temperature during CSS deposition were visibly covered with a white-colored film on the TCO layer, which became more transparent as the temperature increased. All full-well depositions along with their average top heater, bottom source, and calculated substrate temperatures are listed in Table 4.1.

TABLE 4.1. Full-well CuCl CSS deposition runs in the ARDS

Bottom Source [°C]	Top Heater [°C]	Calculated Substrate [°C]	Sticking Coefficient S
210.0	171.0	180.6	0.9381
210.1	180.6	187.9	0.9623
210.1	186.0	191.7	0.8493
210.0	191.0	195.4	0.5598
210.0	210.9	210.7 ¹	0.0067
199.9	171.0	177.9	0.5929
200.1	175.1	181.0	0.5016
200.1	180.8	185.3	0.3645
190.1	166.5	172.1	0.3230
190.1	170.8	175.3	0.2486
190.1	176.2	179.4	0.2013

As explained in Section 3.4, 150 points were used to measure the CuCl impingement rate across the substrate wall boundary. The average impingement rate across position 5 (see Figure 3.5a) of the virtual substrate was determined for all simulations. It was noticed that there was minimal change to the value as the substrate temperature increased, therefore the impingement rates shown in Table 4.2 were those typically computed with respect to a given source temperature.

TABLE 4.2. Simulated CuCl impingment rate Φ [nm/s] at each source temperature

Bottom Source [°C]	Φ [nm/s]
210	0.0347
200	0.0182
190	0.0093

CuCl simulated thicknesses observed from these impingement rates had larger magnitudes in comparison to the experimental values. This is due to the sticking coefficient on the substrate being less than unity, meaning that not all CuCl vapor molecules impinging on the surface adsorb to it. Therefore by dividing all experimental adsorption rates by the simulated impingement rates at a given bottom source temperature, a sticking coefficient as

¹Experiment used to verify that no deposition would occur when all temperatures were approximately the same

a function of temperature was recorded in order to systematically converge the simulation model to the experimental results. Several logistic curve fits were computed using sticking coefficients found at each full-well deposition run (see Table 4.1). Equation 4.1 denotes the logistic S curve fit found for each source temperature:

$$(4.1) \quad S(T) = \frac{1}{1 + \alpha \cdot \exp\left(\frac{\beta}{R(T_{substrate} - T_{source})}\right)}$$

where α and β are fitted parameters and the temperature variables are in Kelvin. Table 4.3 refers to the parameter values based off of the source temperature. The sticking coefficient values were grouped in this manner for clarity of the relationship between thermal conditions of the substrate and bottom source and how each of them affects CuCl growth. Although a detailed physical explanation has not yet been discovered for each of the curves, the general concept is that α loosely defines the mechanism by which molecules accumulate or get rid of excess energy [36] while β is more closely related to the activation energy of the adsorbed CuCl molecules to the TCO surface. T_{source} in the denominator of the exponential function is included so that an asymptotic cutoff can be establish when the substrate temperature is greater than the bottom source temperature. In essence, no sticking will occur ($S = 0$) on the substrate when $T_{substrate} > T_{source}$. The simulation accuracy was improved by applying the S curve fits in Figure 4.1 to the original simulated thicknesses. From a general perspective, the S curve fit plot as well as impingement rates found in Table 4.2 are beneficial tools that can be used in future deposition runs to determine the adsorption rate of CuCl at some given CSS thermal condition. They eliminate the need for costly trial and error experiments to find a suitable CuCl average thickness. The method for calculating S can be extended to virtually any material as long as enough experimental values are recorded to establish the appropriate α and β fitting parameters.

TABLE 4.3. S curve fitted parameters used for each source temperature

Bottom Source [°C]	α	β
210	4.886e-4	895633.7
200	0.1143	334909.5
190	0.8913	136154.0

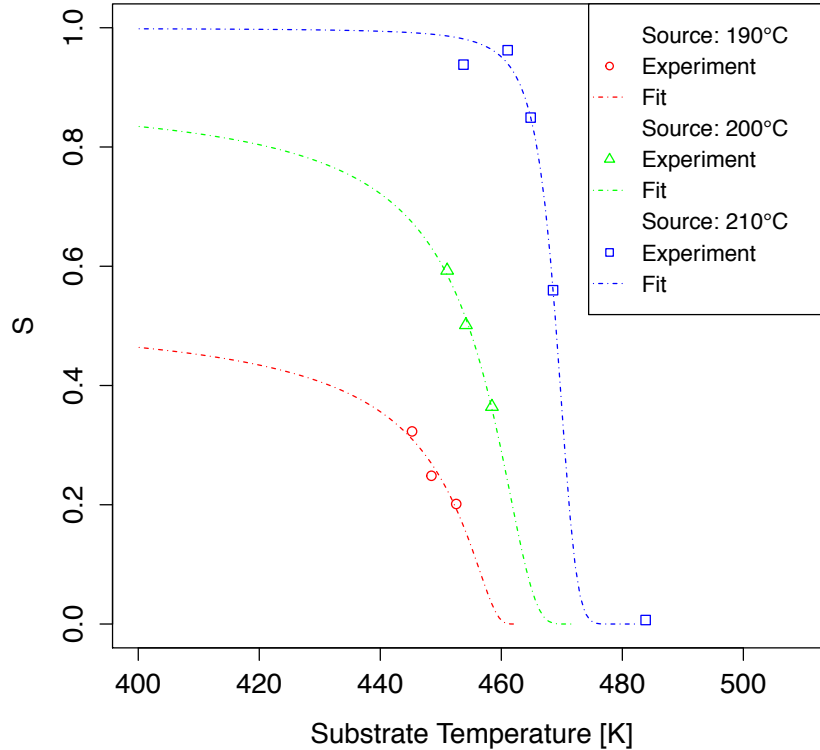


FIGURE 4.1. S curve fits at each source temperature using equation 4.1.

All full-well deposition runs and simulated thicknesses are shown in Figures 4.2a - 4.2c². It is worth noting that the scales for each plot are not the same to avoid any confusion between some conclusions on particular data sets. Analyzing only the experimental results, several descriptive qualities appear within the CuCl thickness. It is apparent that the thermal gradient between the substrate and bottom source will contribute to how thick the CuCl thin-film layers will become. However, there is a limitation to its effect on the adsorption

²Any error bars presented for CuCl thickness are summarized as follows: Horizontal = measurement error from expected crater location; Vertical = interpolated thickness error determined by shift in crater location

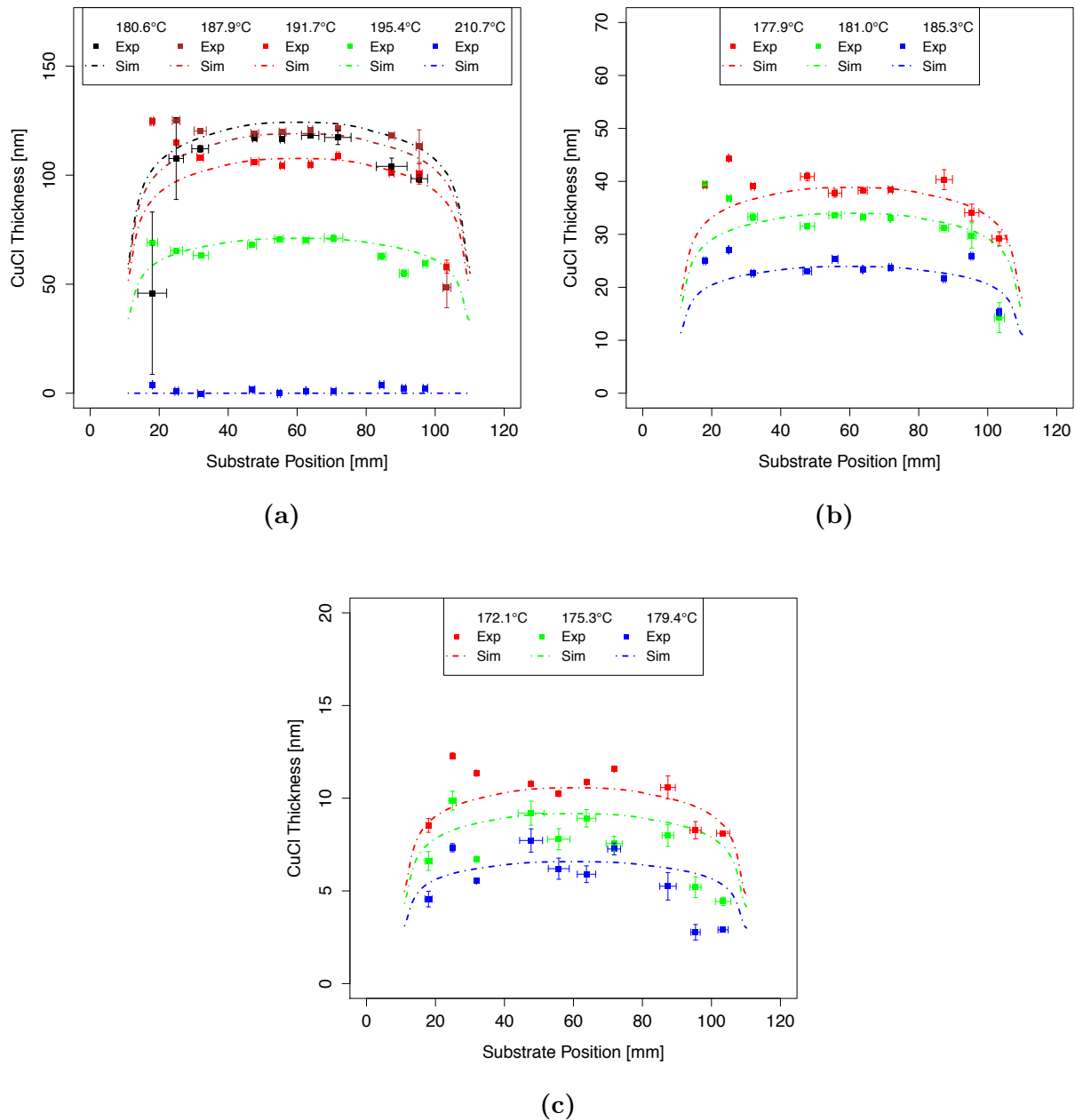


FIGURE 4.2. Full-well deposition experimental and simulated thicknesses at a source temperature of (a) 210, (b) 200, and (c) 190°C

rate dictated by the sticking coefficient. This means that once the sticking coefficient S reaches unity, the adsorption rate will remain constant regardless of how large the thermal gradient becomes when the source temperature is unchanged. A much more influential parameter according to these plots is the source temperature. The CuCl thin-films become

much thicker when the source temperature increases from 190°C to 210°C due to an increase in the sublimation rate. Because of the larger sublimation rate, a higher CuCl vapor pressure would exist near the exposed substrate face that promotes more CuCl to adsorb on it. This is further validated by noticing that the gas species concentration in equation 2.4 is linearly dependent to the overall impingement rate while the substrate temperature only has a square root dependence. It is evident that the source temperature, and thus the amount of CuCl gas in the pocket, is one of the major driving forces to CuCl growth.

Another notable characteristic in the results is the slightly thicker CuCl film on the left side of several substrates (15-35 mm range on the substrate position, or Position 3). Thermocouples placed on the bottom source and shielding surrounding the side of the CSS domain revealed two things: 1) the CuCl bottom source had a temperature gradient of 1°C and thus was assumed to be thermally uniform, and 2) a significantly larger thermal gradient of 13-15°C was measured from the right face to the left face of the shielding. This gradient was due to the overall temperatures in the domains directly adjacent to the CuCl domain. On the side where the CuCl film appeared to be thicker, an “open” domain sat next to the CuCl domain and contained no thermal sources that drove it to a specified temperature. On the other side, however, the “anneal” domain used for Cu annealing was maintained at 200°C during deposition. The thermal gradient across the side shielding was initially thought to explain why the substrate position adjacent to the open domain was thicker than the position closer to the anneal domain. An attempt to validate this proposition was made by running a FLUENT thermal simulation with the thermocouple data³ and emissivity specified for the shielding and source materials [37–39]. Despite this obvious difference in shielding temperatures, the simulation showed no significant thermal non-uniformity on the

³Details of the thermocouple experiment and thermal simulation model can be found in Appendix B

substrate ($\approx 0.2^\circ\text{C}$). More analysis needs to be done before deciding that the thickness non-uniformity is due to a thermal gradient in the domain. Another plausible explanation for the thicker side would be the existence of gaps between the substrate and end effector that holds it. There is a noticeable tolerance between the two, which may force CuCl vapor to escape from the sides and potentially lead to slightly higher local area deposition on the perimeter of the substrate rather than the center.

The most notable characteristic for the experimental results of CuCl growth is the non-uniformity of deposition across the substrate diagonal as seen in Figure 4.2c. It appears that island formation is occurring in various regions at all substrate temperatures, proving that the CuCl condensed molecules prefer to stick together rather than form layers across the FTO coated substrate. Such peaks and valleys seen across the substrate diagonal indicate that the CuCl growth mechanism favors Volmer-Weber growth.

Evaluating the simulation results, the predicted average thicknesses were very close to the observed experimental values after applying the S curve fits to the initial simulation data. However, it is evident that the non-uniformities seen in the experimental results were not replicated by the simulation despite the average thickness correlations. Each full-well deposition run displays some type of roughness due to grain coalescence and islanding on the surface. The current model simply assumes the entire substrate is at a uniform temperature and does not factor in other kinetic interactions (i.e. diffusion, migration, impingement orientation) or surface conditions on the TCO layer. This limitation is inherent in all continuum-based programs like ANSYS[®] FLUENT and is thus only capable of finding an approximation of CuCl adsorption unless further user-defined functions are created to somehow account for these discrepancies. Nonetheless, the current model used the S curve

fit results found in the full-well case to verify its capability in predicting CuCl thin-film deposition and growth in an extreme process condition via single-well deposition.

4.2. SINGLE-WELL DEPOSITION

Single-well depositions were implemented in the CuCl growth study to determine whether the physical description of CuCl vaporization within the model was upheld during a vastly different process condition. By using only one well filled with CuCl rather than all 20 wells, this particular set of experiments would also further elucidate the dominant growth mechanism in CuCl on the TCO layer. Table 4.4 presents the single-well runs along with the calculated substrate temperatures at each top heater and bottom source thermal condition. Temperatures were chosen to match the conditions of the full-well case within reasonable tolerance to compare thicknesses. Using the same mesh geometry as the full-well case, the simulated thickness was quantified with the sublimation mechanism enabled on a single well source. Figures 4.3a - 4.3c provide the single-well deposition results for both the ARDS experiments and FLUENT modeling simulations. The simulation thicknesses were again multiplied by the S curve fits in Figure 4.1 depending on the substrate and source temperatures used in the deposition run.

TABLE 4.4. Single-well CuCl CSS deposition runs in the ARDS

Bottom Source [°C]	Top Heater [°C]	Calculated Substrate [°C]
210.0	176.0	184.2
210.0	181.0	187.9
210.0	186.0	191.7
200.1	170.7	177.7
200.0	175.6	181.4
200.0	181.0	185.4
189.9	166.0	172.1
190.0	171.3	175.7
190.0	175.3	178.7

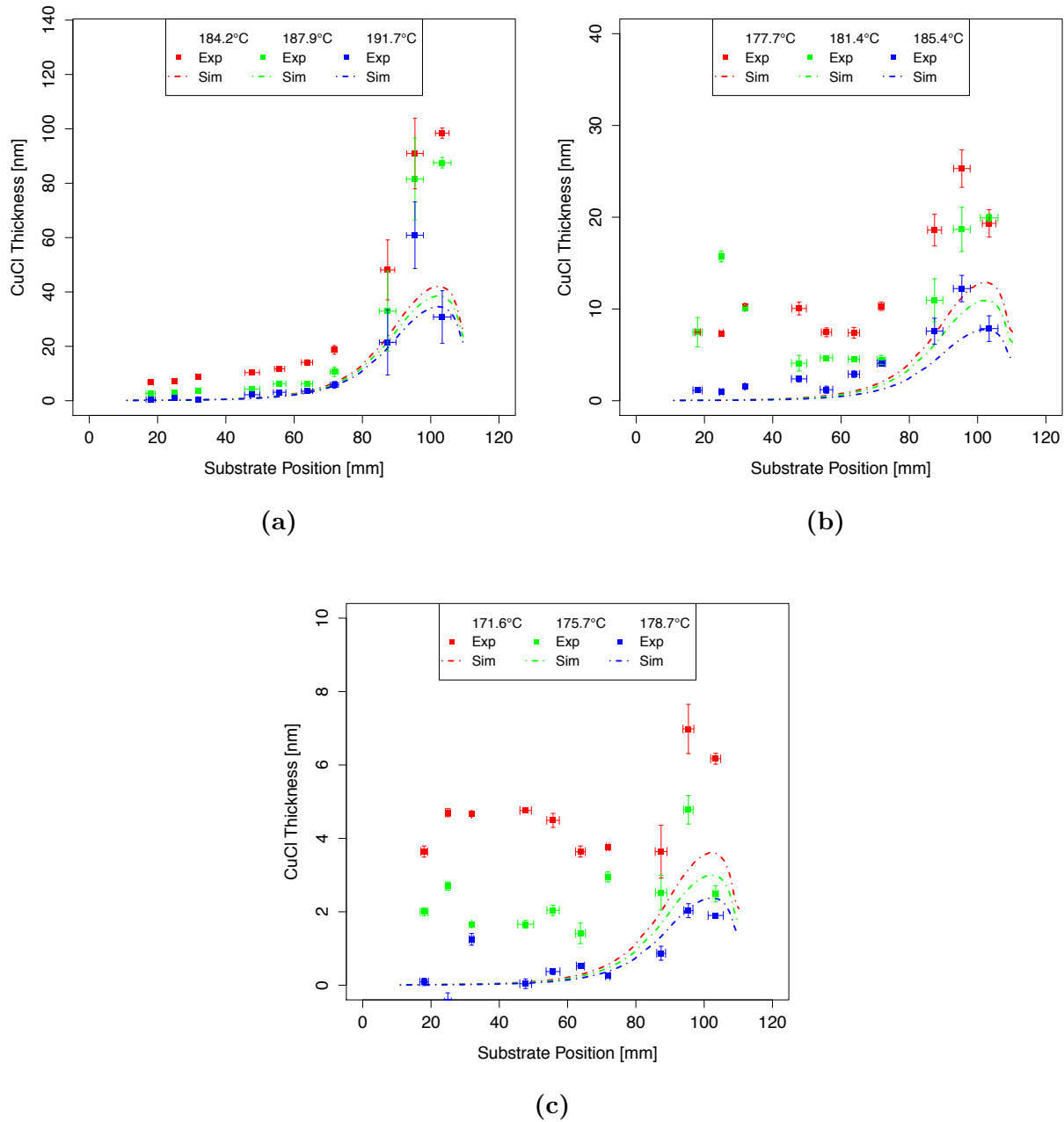


FIGURE 4.3. Single-well deposition experimental and simulated thicknesses at a source temperature of (a) 210, (b) 200, and (c) 190°C

It was expected that the CuCl simulated thickness would be comparable to the experimental thickness as seen during the full-well case. However, the maxima of the single-well simulated thicknesses were found to be significantly lower than the experimental maxima results by an averaged factor of 1.79, regardless of source temperature. The primary reason

that may explain such a discrepancy is related to a vapor pressure effect in the pocket. Since the CuCl partial pressure is restricted to the volume of the pocket, no further sublimation could take place without some type of deposition occurring on the CuCl domain walls or until the substrate entered the domain. The greater number of sublimating wells in the full-well case would be closer to the partial pressure saturation point, which would limit the amount of sublimation. In contrast, the single-well sublimation case may not reach a saturated pressure because the deposition rate on the substrate surface after entering the domain is greater than the sublimation rate required to achieve an equilibrium vapor pressure. In turn, this would cause most of what sublimates from the single well to adsorb to the substrate and give a thickness near the full-well case. Considering these effects, the current simulation model does not accommodate this limitation since it only uses the empirical sublimation rate determined from the mass-loss experiment in Section 3.2. The B_1 and C_1 terms in equation 2.14 do not incorporate the changes in vapor pressure as expected. Thus an equation that includes a pressure-dependent term is necessary to describe the changes to sublimation due to CuCl vapor pressure⁴.

The second reason relates back to the growth mode of CuCl on the TCO layer. If the CuCl overlayer preferentially forms islands, this would lead to a higher sticking probability in isolated regions on the substrate and would dictate grain growth even if a uniform vapor pressure was achieved in the pocket. This can be seen by looking at how CuCl growth seems to occur in areas not directly in the line of sight of the filled CuCl single-well source. In contingency with this result, all experiments had substantially thick, non-uniform films in positions 3 and 5 of the substrate diagonal, especially for experiments in Figures 4.3b and 4.3c. Once again, the Volmer-Weber growth mechanism is the most plausible explanation

⁴See Appendix C for more details

for this island growth of CuCl. Another explanation for this phenomenon is related to secondary diffusion of the CuCl molecule that has not stuck to the surface. It is possible that any of the impinging molecules that either desorb or reflect from the substrate may enter the vapor species and diffuse further across the substrate and adsorb at a later time. A more in-depth study on this effect needs to be done though to see how much it contributes to island formation.

The aforementioned reasons explain why the simulated thicknesses are much smaller than the experimental values in all single-well cases. The model did not predict any of the islands forming on the surface nor did it accurately represent the vapor pressure effects that caused the actual thicknesses to be similar to the full-well case despite less wells being filled. It is obvious that there are major complexities that are unaccounted for in the current model of CuCl thin-film growth and thus further refinement must be done to the simulation model. It is necessary to implement both the CuCl growth mechanism and a vapor pressure term to improve modeling accuracy of CuCl thin-film deposition.

4.3. SEM/EDS ANALYSIS

Despite other research studies evaluating the thin-film growth mode of CuCl deposited on various substrate materials [19, 20, 40, 41], it was not known if similar behavior during CSS would be prevalent for CuCl on the FTO layer. To assess the growth characteristics of CuCl, SEM and EDS were performed on the full-well experiments in order to visually analyze the effects of modulating the thermal conditions at both the substrate and source. The following subsections will elaborate on the perceived trends that distinguish the CuCl thin-film deposition and main growth mode responsible during CSS.

4.3.1. SEM ANALYSIS. The growth mechanism of CuCl during the substrate temperature sweep was investigated using Scanning Electron Microscopy on position 8 of each substrate sample (please refer to Figure 3.5). SEM was operated at 15 kV accelerating voltage at 30,000 \times magnification for all samples to keep consistency in visual comparison. Figures 4.4a reveal the CuCl grains imaged when the substrate temperature was increased from 180 $^{\circ}$ C to 210 $^{\circ}$ C while maintaining a source temperature of 210 $^{\circ}$ C. Grains in Figure 4.4a are fully coalesced with few gaps between each large grain network. As the substrate temperature increases (Figures 4.4b - 4.4d), the grain networks shrink toward the centers of each grain and separate into regions of CuCl islands. As the substrate temperature approaches the source temperature, CuCl vapor molecules no longer adsorb to the surface and as a result leave a barren TCO layer (Figure 4.4e). To verify that Figure 4.4e is in fact the TCO layer, a blank TEC-12D substrate was imaged as a means of validation (Figure 4.4f). As expected, the TCO layers match from a visual perspective and are vastly different from the CuCl grains seen in previous images.

Figures 4.5a - 4.5c depict the CuCl thin-film growth at a source temperature of 200 $^{\circ}$ C and an increasing substrate temperature from 175 to 185 $^{\circ}$ C. Since the substrate temperatures are closer to each other for this data set compared to the previously mentioned substrates at a 210 $^{\circ}$ C source temperature, there are not striking differences between grain size. However, in comparison to Figures 4.4a - 4.4e the grains have become smaller and appear to have nucleation regions scattered between islands. Furthermore, as substrate temperature increases there are slightly less CuCl grains across the imaged region.

The last full-well deposition runs were performed at a source temperature of 190 $^{\circ}$ C with a varied substrate temperature from 170 to 180 $^{\circ}$ C (Figures 4.6a - 4.6c). The CuCl grains are much smaller than the higher source temperature depositions, showing the influence of

the CuCl vapor species concentration on the overall thin-film growth. It is evident that the onset of CuCl nucleation is occurring since the CuCl islands have greatly diminished and the TCO layer below is visible throughout the imaged region.

4.3.2. EDS ANALYSIS. EDS was performed in conjunction with the SEM images to help support the claim that CuCl preferentially grows as island formations across the TCO layer. This characterization technique was necessary in differentiating between CuCl islands and the SnO layer beneath them by assessing the elemental composition of the imaged region. All EDS results were performed at 7.5 kV accelerating voltage with a 20,000 \times magnification and drift correction enabled. Figures 4.7a - 4.7e display the mapping analysis of Cu, Cl, Sn, and O normal to surface with respect to substrate temperature. The general trend shows the CuCl grains shrinking and SnO signals expanding between islands as the surface temperature increases toward the source temperature, whereupon in the final stage Cu and Cl signals are undetectable. Again, coalescence is prevalent at lower temperatures while individual CuCl islands exist at higher temperatures.

Overall the Cu and Cl signals in Figures 4.8a - 4.8c correlate with each other in their mapped locations, indicating that the molecule is most likely non-dissociative during adsorption as assumed. This set of deposition runs had much smaller islands than previous EDS images, which is in agreement with the expected trend of thinner CuCl films with decreasing source temperature. The grains also become fewer with increasing substrate temperature. As the source temperature decreases to 190°C (Figures 4.9a - 4.9c), the Cu and Cl signals disappear until there is minimal Cu on the surface with only Cl leftover on the Sn and O rich areas. Such tiny grains are indicative of the onset of nucleation prior to island-by-island formation as seen in previous results, which again leads back to the conclusion that the Volmer-Weber growth mode is responsible for such growth.

4.3.3. SUMMARY. Evaluating all of the SEM/EDS images for full-well depositions elucidates a number of CuCl growth characteristics. It is obvious that as the substrate temperature increases, the CuCl grain size decreases with islands becoming more prominent versus layer-by-layer films seen in Stranski-Krastanov growth [42]. This phenomenon is in contrast to that observed during the studies on CuCl/MgO interfaces [19, 20], and thus the results in this research suggest that the Volmer-Weber growth mode seen in the SEM and EDS images is the dominant interaction mode between CuCl adsorbed molecules on a Fluorine-doped Tin Oxide layer. Such a growth mode is not favored in other thin-film semiconductor materials used in the ARDS such as CdS, which typically exhibits an S-K growth mode [43]. Therefore it becomes increasingly important to control how much Cu is used to dope the CdTe absorber layer. Despite this being a 2nd or 3rd order contributor to the Cu doping issue, too much CuCl impinging on the CdTe surface may lead to Cu island non-uniformities at the exposed CdTe interface. It is possible that the Cu would diffuse into CdTe at higher concentrations where island formation is prominent, resulting in non-uniform carrier transfer regions that may decrease solar cell efficiencies. However, this is merely speculation based off of the current findings and requires much deeper characterization analysis to understand in detail. Furthermore, this research study only focused on the CuCl/TCO interface rather than extending it to CuCl/CdTe, which is the primary deposition sequence in the ARDS. The reason for studying the former in detail was to gain a general understanding of CuCl thin-film growth without the added complexity of species diffusion or migration that exists in the latter case. Nonetheless, the CuCl thin-film growth results for SEM/EDS reveal that Volmer-Weber growth is the mode responsible in CuCl thin-film deposition within the CSS process.

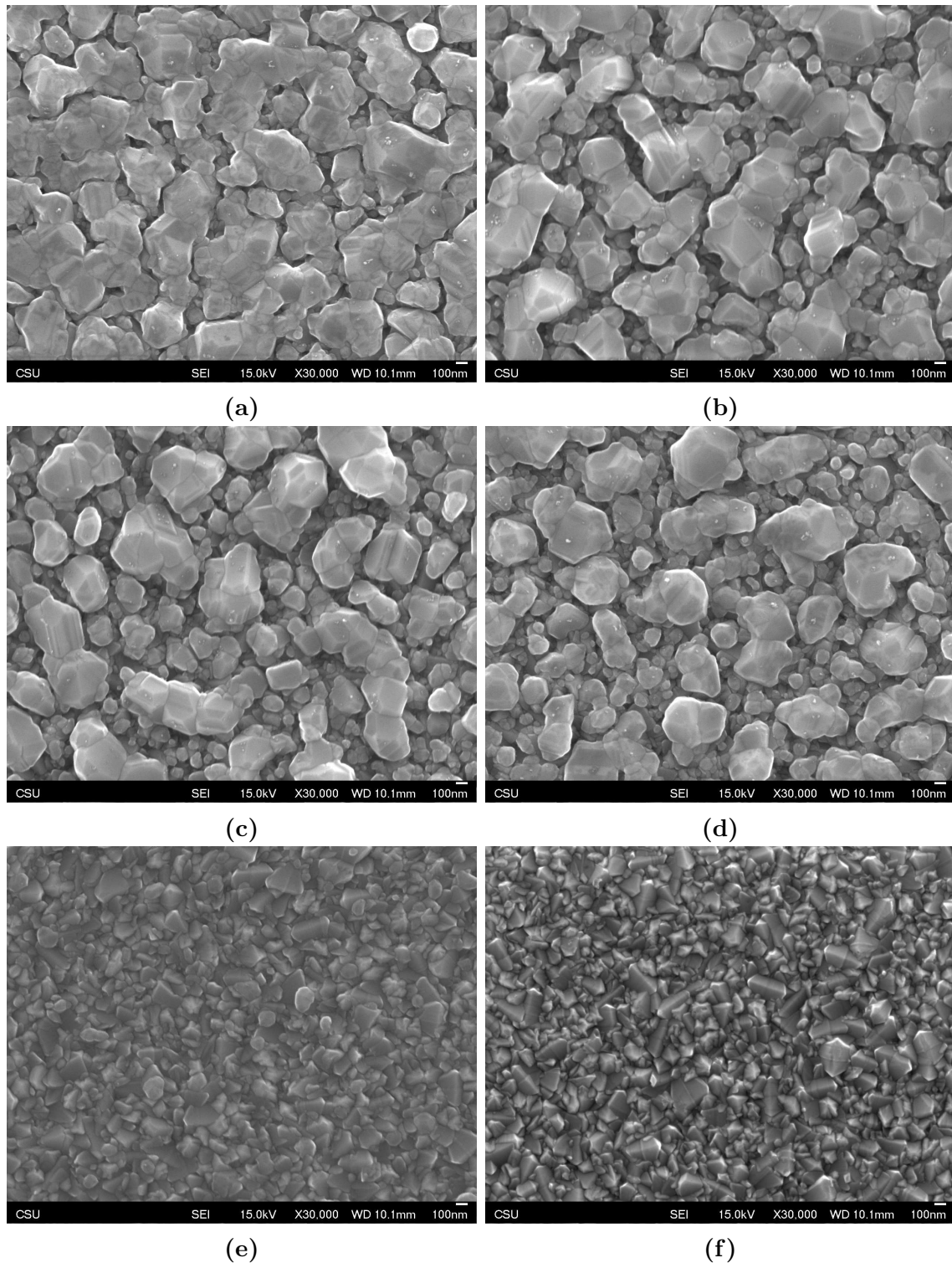
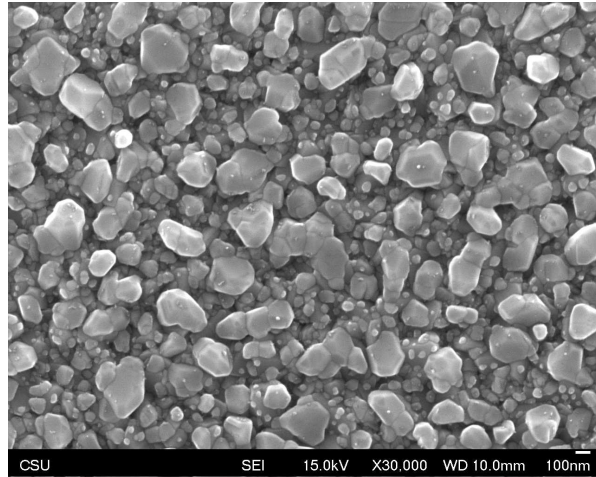
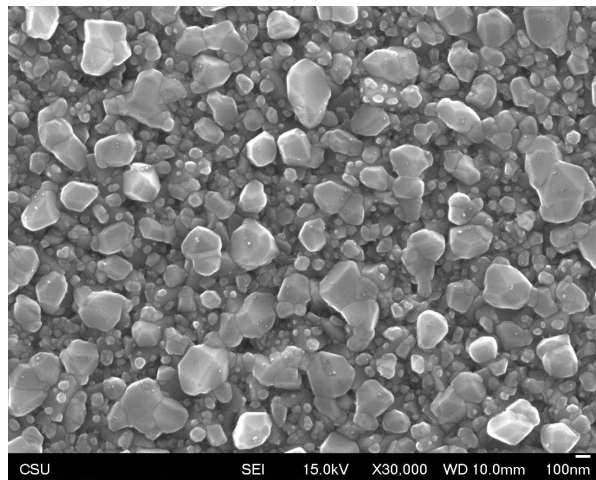


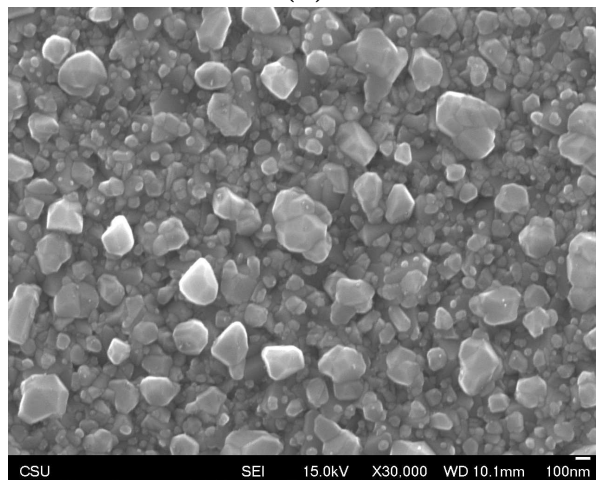
FIGURE 4.4. SEM images for source temperature = 210°C and substrate temperature = (a) 180.6, (b) 187.9, (c) 191.7, (d) 195.4, and (e) 210.7°C. (f) SEM image of TCO layer only on TEC-12D substrate (no deposition) as a visual comparison with (e). The scale on the bottom right of each image is 100 nm.



(a)

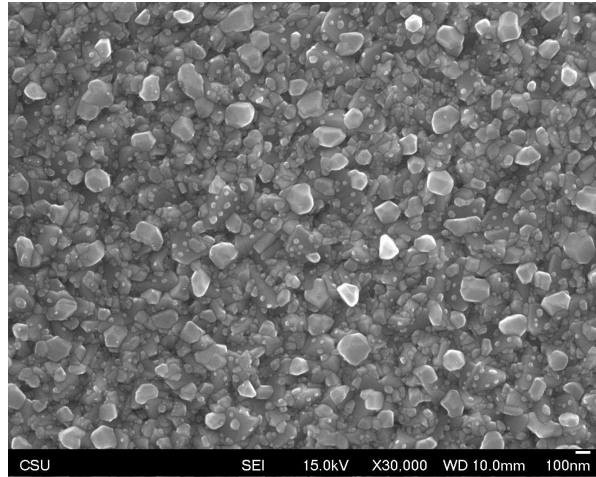


(b)

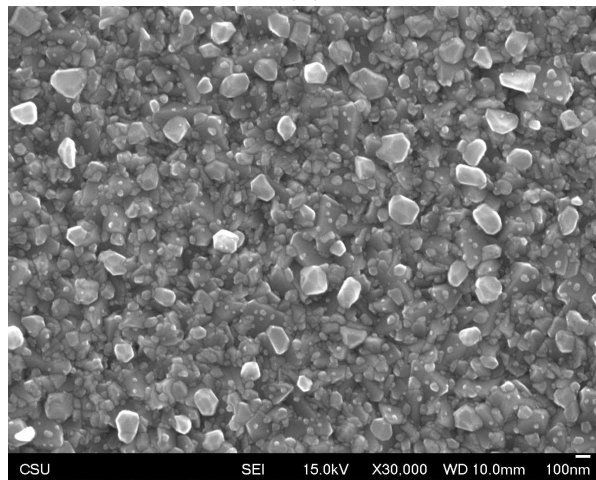


(c)

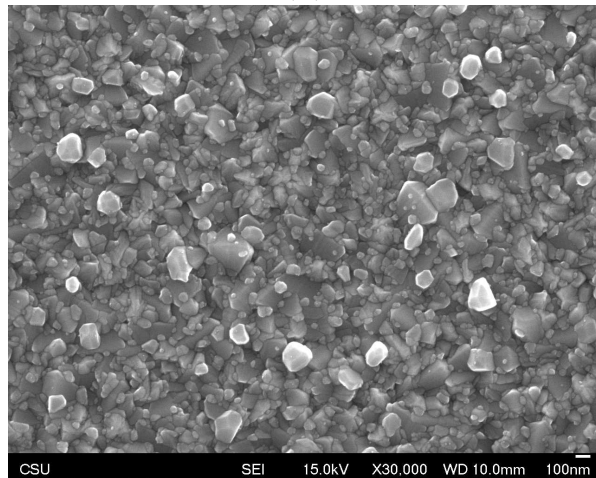
FIGURE 4.5. SEM images for source temperature = 200°C and substrate temperature = (a) 177.9, (b) 181.0, and (c) 185.3°C. The scale on the bottom right of each image is 100 nm.



(a)



(b)



(c)

FIGURE 4.6. SEM images for source temperature = 200°C and substrate temperature = (a) 177.9, (b) 181.0, and (c) 185.3°C. The scale on the bottom right of each image is 100 nm.

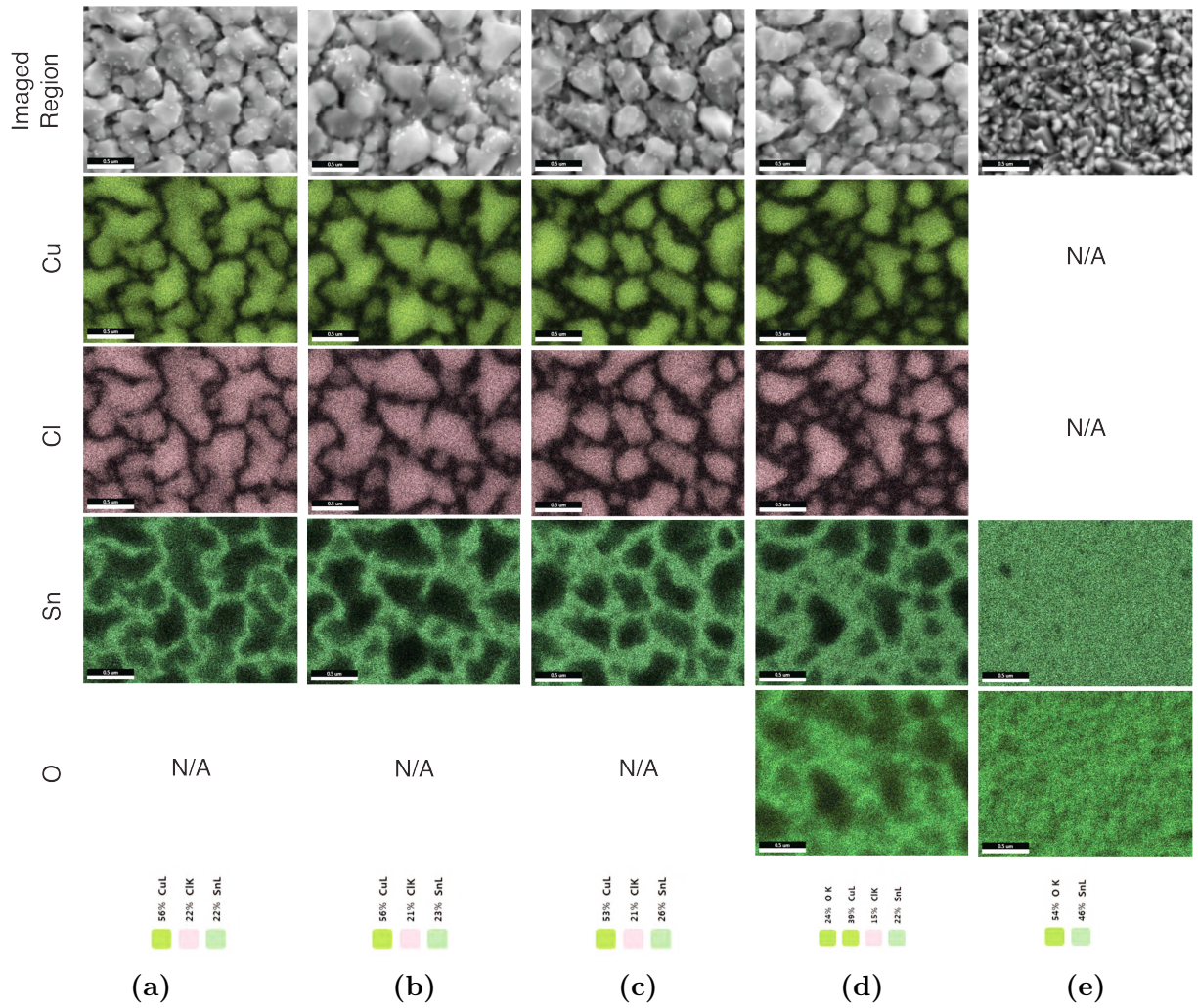


FIGURE 4.7. EDS images for source temperature = 210°C and substrate temperature = (a) 180.6, (b) 187.9, (c) 191.7, (d) 195.4, and (e) 210.7°C. The scale at the bottom left of each image is 0.5 μm .

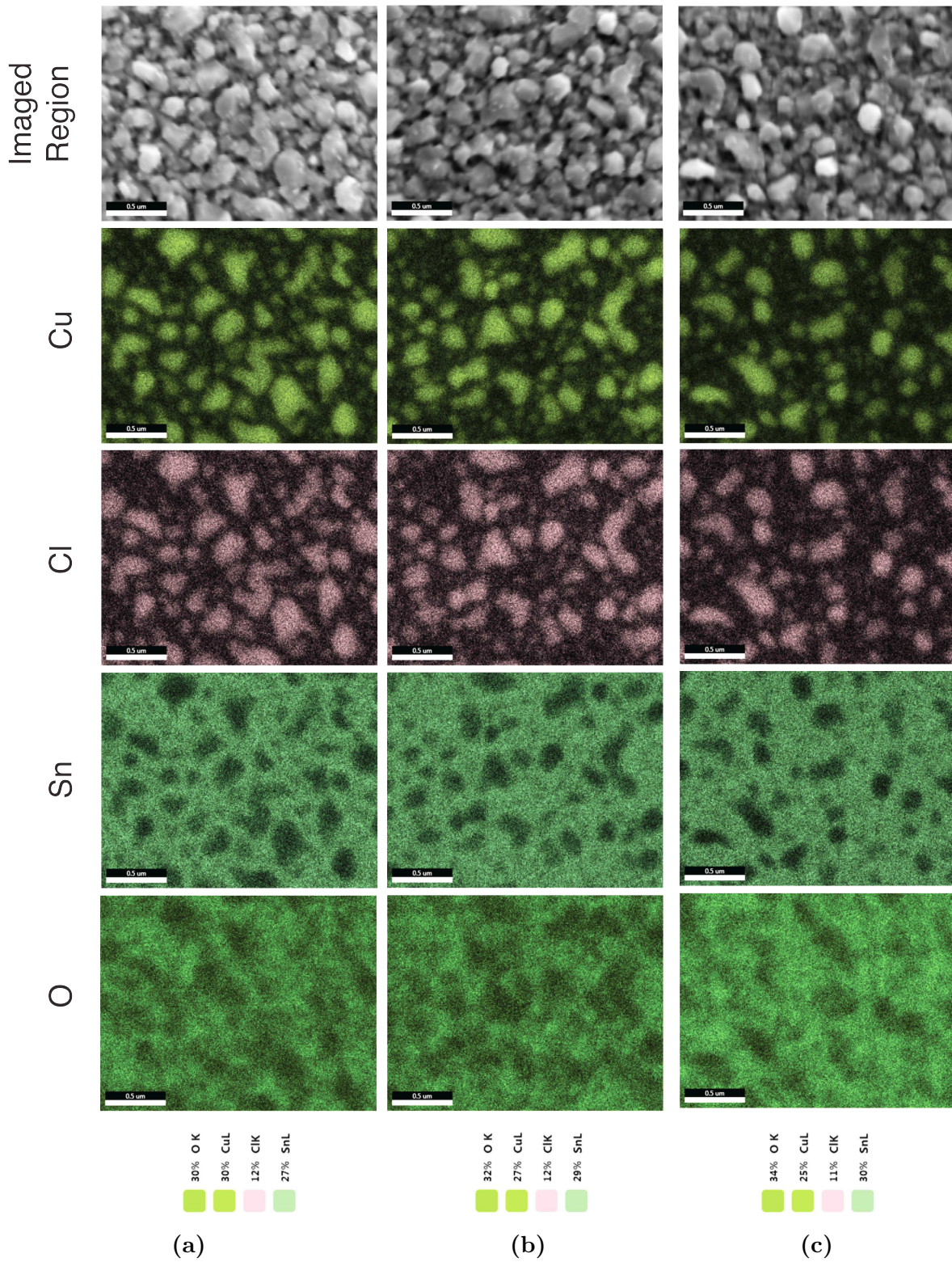


FIGURE 4.8. EDS images for source temperature = 200°C and substrate temperature = (a) 177.9, (b) 181.0, and (c) 185.3°C. The scale at the bottom left of each image is 0.5 μm .

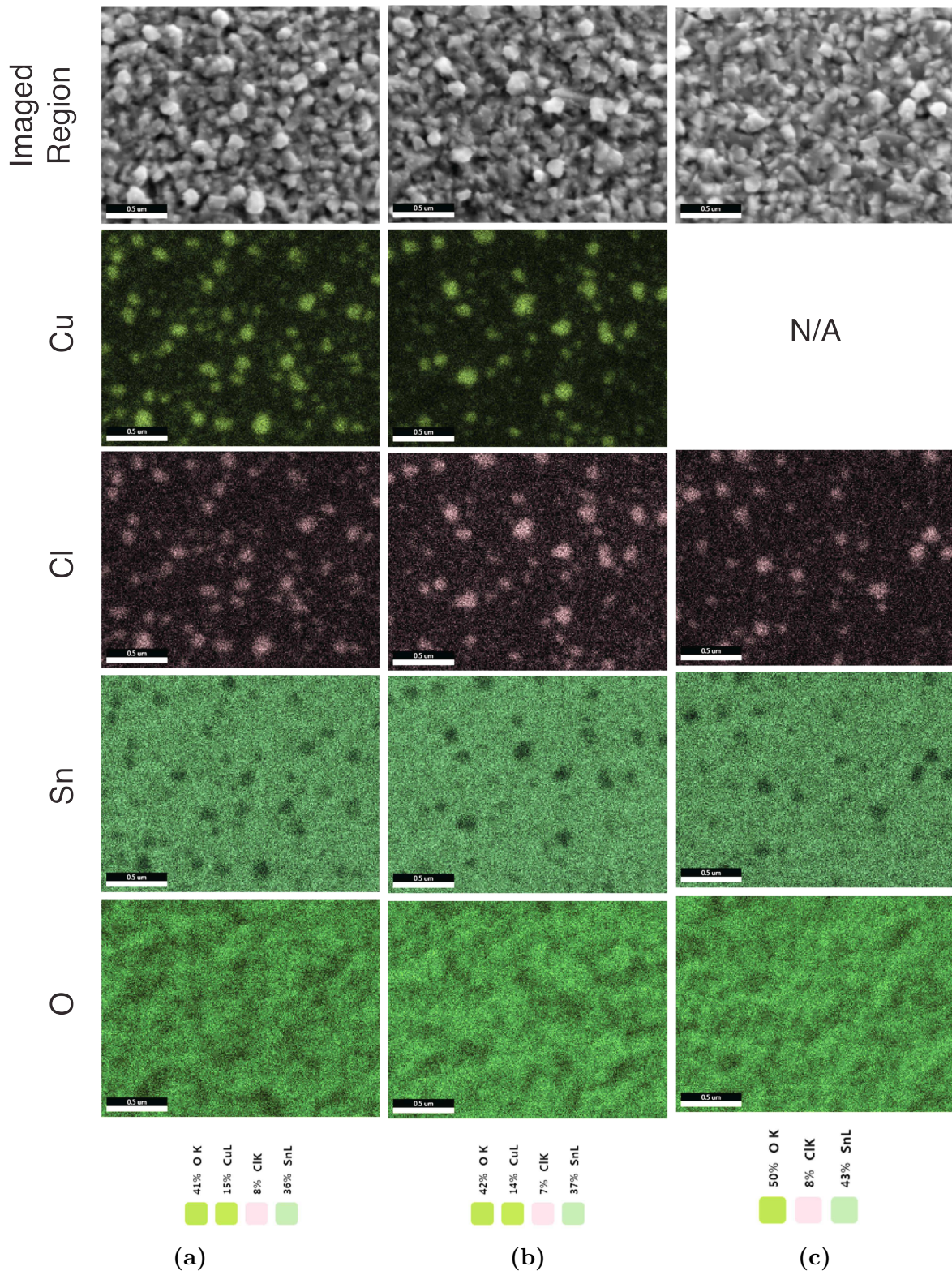


FIGURE 4.9. EDS images for source temperature = 190°C and substrate temperature = (a) 172.1, (b) 175.3, and (c) 179.4°C. The scale at the bottom left of each image is 0.5 μm .

CHAPTER 5

CONCLUSION/FUTURE WORK

5.1. CONCLUSION

CuCl thin-film growth was explored while varying CSS thermal parameter conditions. By gaining insight on how CuCl deposits on the substrate, a general assessment could be developed as to what heating temperatures within the CuCl domain will give the most uniform deposition across the entire substrate. The uniformity of Cu doping in the CdTe absorber layer has been a challenging issue within thin-film solar cell fabrication. The ultimate goal for this study was to devise a means of predicting the CuCl uniformity within the ARDS that would lead to an overall understanding of the CuCl vaporization process. The computationally accurate model would then be used to determine a CSS operation range capable of achieving an optimal solution for Cu doping in the CdTe absorber layer.

Results on the CuCl mass-loss experiment point out the necessity of obtaining an Arrhenius expression for the CuCl sublimation rate at a higher pressure regime than most literature [7, 27–29]. Such a study was crucial in providing an accurate kinetic vapor rate in CSS modeling because of its direct contribution to the impingement rate as shown in equation 2.4. With such data, a more representative species concentration was seen within the CuCl pocket that proportionally changed the deposition rate on the substrate mesh boundary. Furthermore, the derived Arrhenius expression was used for several source temperature values so that a wide range of simulations could be completed with minimal inputs by the program user. In spite of the CuCl mass-loss data found for the full-well case, applying the same Arrhenius expression to the single-well modeling case and comparing to the experimental results demonstrated a significantly less sublimation rate than the latter. It was

speculated that the single-well experiment did not completely reach an equilibrium vapor pressure in the pocket since the already low CuCl gas concentration was rapidly deposited on the substrate. This would consequentially drive the single well source to further sublimation to compensate for the lack of a saturated pressure condition. Such circumstances would explain why more sublimation would occur and thus give a higher CuCl thickness measurement than the model originally proposed. The single-well modeling results prove that the CuCl model in an extreme deposition case was not quantitatively accurate and thus requires more development to become a high-fidelity computational simulation.

The full-well simulations and experiments were used to determine an S curve fit for each particular source temperature. All sticking coefficients for a given substrate temperature were found using equation 2.5 with the experimental adsorption rate and calculated impingement rate as inputs. Equation 4.1 was then fitted to the sticking coefficient values at various substrate and source temperatures and applied to each full-well simulation model for further computational accuracy. The model was able to converge to the average CuCl thickness experimental results but could not accurately represent the thickness non-uniformities present in all experiments. This is due to the simplistic modeling conditions at the substrate wall, which lack a growth mode algorithm that enables dynamic interaction between the gas and site species on its boundary (i.e. nucleation, islanding, percolation, and coalescence). A number of CuCl depositions were relatively thicker on position 3 of the substrates and may indicate that some type of gradient exists in the pocket. However it is not exactly known whether a substrate temperature or species concentration gradient is responsible for the issue. The thermal modeling conducted on the CuCl domain in the ARDS seems to refute the possibility of a thermal gradient across the substrate or the CuCl bottom source. If the thermal modeling results are valid, then the only sound explanation would be some type of

small gap between the substrate and end effector that is causing CuCl vapor to deposit more readily on one side of the substrate.

An in-depth observation of the SEM/EDS results showed that in general the CuCl grains diminish in size and number at higher substrate temperatures. SEM revealed such a pattern when the coalescence of large CuCl grain networks eventually separated into smaller islands with increasing substrate temperatures. EDS mapping further validated this phenomenon by showing the Cu and Cl island signals decreasing with Sn and O counts increasing between island regions. Eventually the Sn and O signals dominated the entire mapped region as the substrate temperature reached the source temperature. Across lower source temperature mappings, the grains were significantly smaller than the largest source temperature data and consistently depicted nucleation islands as oppose to uniform CuCl layers. In summary, CuCl thin-films grown on FTO-coated substrates exhibit the Volmer-Weber growth mode by first forming islands and then coalescing to develop large grain networks across the exposed surface.

Following the full-well CSS experiments, single-well deposition runs were performed to check the fidelity of the simulation model in an extreme process condition. It was concluded that the model did qualitatively predict the hill-top shape of single-well CuCl thin-film growth but did not effectively represent the varying surface topologies displayed in most single-well CuCl experiments. The current simulation model can at the very least provide an accurate computation of the CuCl sublimation process that predicts the average CuCl thickness based on the CSS thermal conditions. This demonstrates that the CFD-based CuCl thin-film growth simulation during CSS is moving in the right direction and can be improved for more complex kinetic phenomena or applied to various domain geometries.

5.2. FUTURE WORK

There are many opportunities to enhance the current simulation model. The discrepancies between the predicted thickness and the experimental results is mainly due to the lack of particle surface interactions that occur on a nanoscale. By assuming that the site species remained constant throughout deposition, no method was assigned that accommodated for the roughness across the substrate after CuCl adsorption. In turn, the steady-state solution for the deposition rate remained ideally uniform since there were no influences from adjacent mesh layers over time. One way to integrate a physical change to the wall surface over time would be to create a time-dependent dynamic mesh surface accompanied by a user-defined function that models the growth mode at a given interface. Surface energies at each node of the substrate wall and dimensional cell parameters such as tilt angle and face size would be collected and processed with respect to time. CuCl thin-film topologies could then be manipulated on the substrate mesh body, acting in essence as a pseudo-transient surface that changes in response to the fluctuation of CuCl site species at each time step. Such a model would act in place of a molecular dynamics simulation of deposition rate while retaining its continuum-based species algorithms.

Experiments with CuCl deposition to a CdTe layer would be another major next step in this work. CdTe is significantly thicker and rougher than CuCl at only 110 s deposition on the substrate, so it would be necessary to obtain a thin-layered CdTe (≈ 100 nm) with properties comparable to its thicker predecessor. A thin CdTe layer would also make it possible to use the current Argon Ion Beam Sputtering method to measure the crater depths with SWLI. If there is any concern for HCl etching at the bottom CdTe layer, a less aggressive solution such as methanol or IPA could be used in place for removing the CuCl overlayer. After refinement and execution of the previously mentioned simulation improvement, a new mesh

layer interface such as CdTe could be created on the pre-existing TCO mesh to check how the deposition rate changes. Since Cu diffusion and migration would be of interest, inclusion of Te site species that interact with Cu and sink regions that effectively remove the CuCl concentration near the CdTe boundary would be required for accurate diffusion analysis. A FLUENT simulation of the CuCl/CdTe interface would offer the most useful knowledge to the growth rates in this region and how they affect Cu diffusion into CdTe.

Analysis of CuCl thin-film deposition and growth at various process conditions with a computational model demonstrates the versatility of using simulation alongside theory and experimentation in the research process. With the current understanding of thin-film deposition by CSS, it is now possible to extend the modeling structure applied in this research study to other materials or thin-film deposition techniques besides Close-Space Sublimation. It is thus apparent that simulation can play an influential role in thin-film manufacturing processes and open up other avenues of exploration for thin-film deposition and growth.

BIBLIOGRAPHY

- [1] F. Breitenecker and I. Troch, “Simulation Software - Development and Trends,” in *Control Systems, Robotics, and Automation* (H. Unbehauen, ed.), vol. IV, EOLSS, 2009.
- [2] J. D. Anderson Jr., *Computational Fluid Dynamics*. 3rd ed., 2009.
- [3] G. E. Moore, “Cramming More Components into Integrated Circuits,” in *Proceedings of the IEEE*, vol. 86, pp. 82–85, January 1998.
- [4] F. Hosseinpour and H. Hajihosseini, “Importance of Simulation in Manufacturing,” *International Journal of Social, Behavioral, Educational, Economic, Business and Industrial Engineering*, vol. 3, pp. 229–232, 2009.
- [5] D. A. Bodner and L. F. McGinnis, “A Structured Approach to Simulation Modeling of Manufacturing Systems,” in *Industrial Engineering Research Conference*, (Georgia Institute of Technology, Atlanta, GA), 2002.
- [6] D. R. Hemenway, “Computational Modeling of Cadmium Sulfide Deposition in the CdS/CdTe Solar Cell Manufacturing Process,” Master’s thesis, Colorado State University, Fort Collins, CO, 2013.
- [7] D. F. Brestovankysy *et al.*, “Analysis of the rate of vaporization of CuCl for solar cell fabrication,” *Journal of Vacuum Science & Technology A*, vol. 1, pp. 28–33, 1983.
- [8] M. Burgelman and A. de Vos, “Evaporation of CuCl and CuCl₂ for the fabrication of Cu₂S/CdS thin film solar cells,” *Thin Solid Films*, vol. 102, pp. 367–374, 1983.
- [9] T. S. Te Velde, “The production of the Cadmium Sulphide-Copper Sulphide Solar Cell by means of a Solid-state Reaction,” *Energy Conversion*, vol. 15, pp. 111–115, 1975.
- [10] B. E. McCandless and J. R. Sites, “Cadmium Telluride Solar Cells,” in *Handbook of Photovoltaic Science and Engineering* (A. Luque and S. Hegedus, eds.), John Wiley & Sons, Ltd, 2003.

- [11] D. E. Swanson *et al.*, “Single vacuum chamber with multiple close space sublimation sources to fabricate CdTe solar cells,” *Journal of Vacuum Science & Technology A*, vol. 34, pp. 021202–1–021202–6, 2016.
- [12] V. V. Plotnikov, X. Liu, and A. D. Compaan, “Studies of Cu location near the back contact of CdS/CdTe solar cells,” in *Photovoltaic Specialist Conference (PVSC), 2008 IEEE 33rd*, (University of Toledo, Toledo, OH), 2008.
- [13] C. S. Ferekides *et al.*, “An effective method of Cu incorporation in CdTe solar cells for improved stability,” *Thin Solid Films*, pp. 5833–5836, 2007.
- [14] F. Bechstedt, *Principles of Surface Physics*. Springer-Verlag Berlin Heidelberg, 2003.
- [15] A. Grob, *Theoretical Surface Science*. Springer-Verlag Berlin Heidelberg, 2nd ed., 2009.
- [16] J. L. Cruz-Campa and D. Zubia, “CdTe thin film growth model under CSS conditions,” *Solar Energy Materials & Solar Cells*, vol. 93, pp. 15–18, 2009.
- [17] S. Miyamoto, “A Theory of the Rate of Sublimation,” *Bulletin of the Chemical Society of Japan*, pp. 794–797, 1933.
- [18] M. Ohring, *Materials Science of Thin Films*. 2nd ed., 2001.
- [19] A. Yanase and Y. Segawa, “Two different in-plane orientations in the growths of cuprous halides on MgO(001),” *Surface Science*, vol. 329, pp. 219–226, 1995.
- [20] A. Yanase and Y. Segawa, “Stranski-Krastanov growth of CuCl on MgO(001),” *Surface Science*, vol. 367, pp. L1–L7, 1996.
- [21] ANSYS® , *ANSYS FLUENT Theory Guide: Release 14.5*. 2012.
- [22] N. Dongari and A. Agrawal, “Modeling of Navier-Stokes equations for high Knudsen number gas flows,” *International Journal of Heat and Mass Transfer*, vol. 55, pp. 4352–4358, 2012.
- [23] C. Kittel, *Introduction to Solid State Physics*. 8th ed., 2005.

- [24] P. M. Agrawal, B. M. Rice, and D. L. Thompson, “Predicting trends in rate parameters for self-diffusion on FCC metal surfaces,” *Surface Science*, pp. 21–35, 2002.
- [25] K. Singer, A. Taylor, and J. V. L. Singer, “Thermodynamic and structural properties of liquids modelled by ‘2-Lennard-Jones centres’ pair potentials,” *Molecular Physics*, vol. 33, pp. 1757–1795, 1977.
- [26] T. L. Bergman *et al.*, *Fundamentals of Heat and Mass Transfer*. John Wiley & Sons, Inc., 7th ed., 2011.
- [27] R. Madar *et al.*, “Thermodynamic analysis of copper CVD using CuCl as precursor,” *Microelectronic Engineering*, vol. 19, pp. 571–574, 1992.
- [28] D. E. Peterson, *Sublimation Thermodynamics and Kinetics of Cuprous Chloride*. PhD thesis, Monmouth College, Monmouth, IL, 1964.
- [29] R. A. J. Shelton, “Vapour pressures of the solid copper (I) halides,” *Transactions of the Faraday Society*, vol. 57, pp. 2113–2118, 1961.
- [30] P. de Groot, *Optical Measurement of Surface Topography*, ch. 9, pp. 187–208. Springer-Verlag, 2011.
- [31] J. Othman, “Heat and Fluid Flow Analysis in a Molten CuCl Heat Exchanger,” Master’s thesis, University of Ontario Institute of Technology, Oshawa, ON Canada, 2009.
- [32] G. A. Slack, “Pressure and temperature effects on the thermal conductivity of CuCl,” *Physical Review B*, vol. 26, pp. 1873–1883, 1982.
- [33] D. R. Lide, *CRC Handbook*. CRC Press, 84th ed., 2003.
- [34] J. A. Dean, *Lange’s Handbook of Chemistry*. McGraw-Hill, 11th ed., 1979.
- [35] Q. A. Acton, “Gases: Advances in Research and Application,” *Scholarly Editions*, p. 1065, 2011.

- [36] L. Vattuone *et al.*, “Initial sticking coefficient of O_2 on Ag(110),” *Journal of Chemical Physics*, vol. 101, pp. 713–725, 1994.
- [37] Mikron[®], “Table of Emissivity of Various Surfaces.”
- [38] G. Atomics, “Graphite Design Handbook,” September 1988.
- [39] G. A. Greene, C. C. Finfrock, and T. F. Irvine Jr, “Total hemispherical emissivity of oxidized Inconel 718 in the temperature range 300-1000°C,” *Experimental Thermal and Fluid Science*, vol. 22, pp. 145–153, 2000.
- [40] G. Natarajan and S. Daniels, “Growth of CuCl thin films by magnetron sputtering for ultraviolet optoelectronic applications,” *Journal of Applied Physics*, vol. 100, pp. 033520–1 – 033520–5, 2006.
- [41] B. Foy, *Growth and Characterisation of Thin Films of CuCl and Related Materials*. PhD thesis, Dublin City University, Glanevin, Dublin 9, Ireland, 2012.
- [42] A. Baskaran and P. Smereka, “Mechanisms of Stranski-Krastanov growth,” *Journal of Applied Physics*, vol. 111, pp. 044321–1 – 044321–6, 2012.
- [43] D. Hemenway *et al.*, “Using computational simulation to model CdS/CdTe processing in close-space sublimation,” in *Photovoltaic Specialist Conference (PVSC), 2015 IEEE 42nd*, pp. 1–6, June 2015.

APPENDIX A

TECHNIQUE VERIFICATION

A.1. HYDROCHLORIC ACID ETCHING ON TCO

Measuring the CuCl thickness before and after HCl etching required that the TCO layer would not be affected during the etching process. To validate that minimal effects occurred on this layer after crater formation, SWLI measurements were done on several bare TCO with craters already formed in the layer. HCl was then applied to the craters and their depths remeasured. The results shown in Table A.1 and Figure A.1 indicate that there was negligible difference between the TCO crater depths before and after HCl etching. This proves that the current technique only etched away the CuCl layer without damaging the bottom TCO layer and thus gives confidence that the measured crater depths after etching are correct.

TABLE A.1. Average TCO crater depth before and after HCl etching at varied Ar^+ sputtering times

Sputtering Time [min]	Unetched		Etched w/ HCl	
	Avg Crater Depth [nm]	\pm SD	Avg Crater Depth [nm]	\pm SD
2.5	70.4	3.1	70.1	0.4
5	141.4	1.7	143.0	1.7
7.5	245.7	2.9	246.1	4.0

A.2. XPS ARGON ION BEAM SPUTTERING ON CuCl/TCO LAYERS

Through trial and error, it was determined that the Ion Gun operating at a beam voltage of 5 kV and sputtering time of 5 minutes total would create visible craters into the TCO. In order to verify that the Argon Ion Beam sputtered deep enough into both the CuCl and TCO layers from a typical CuCl deposition run, X-ray Photoelectron Spectroscopy (XPS) was performed before and after crater formation in the CuCl/TCO layers. To evaluate the

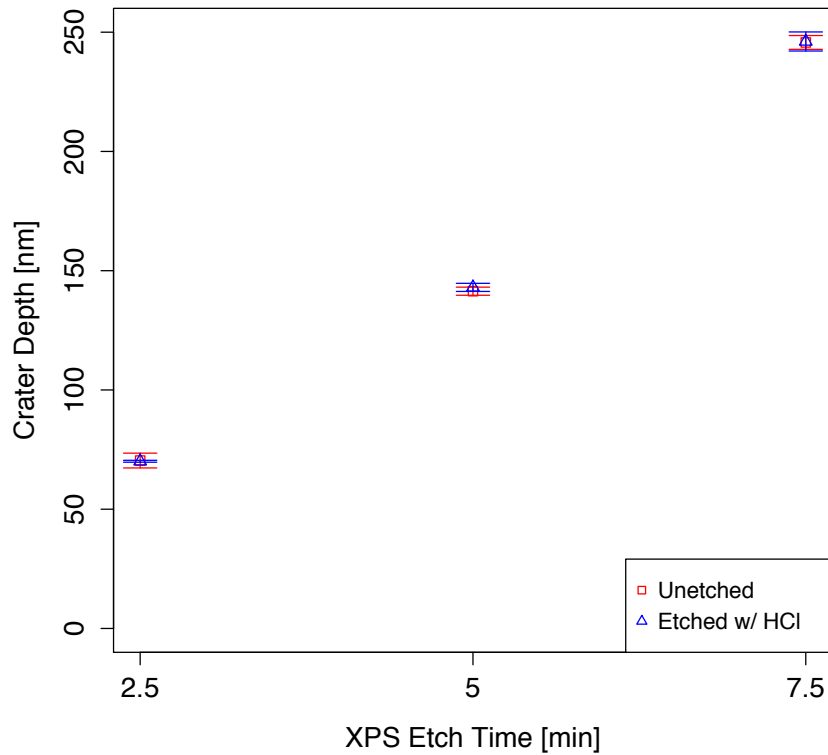
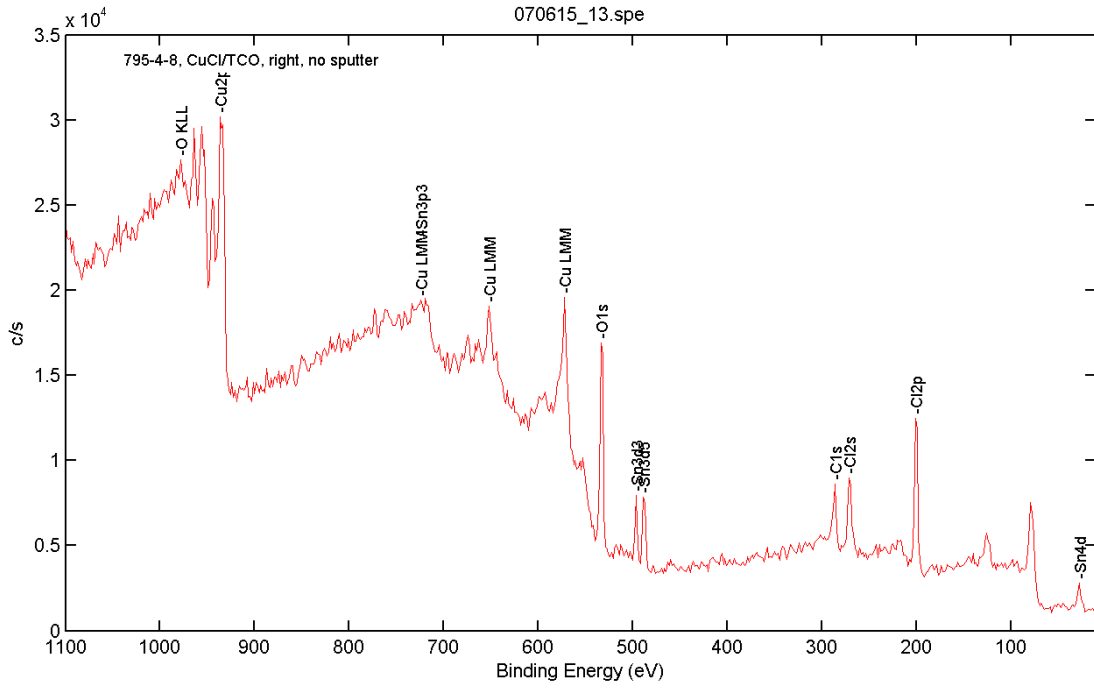
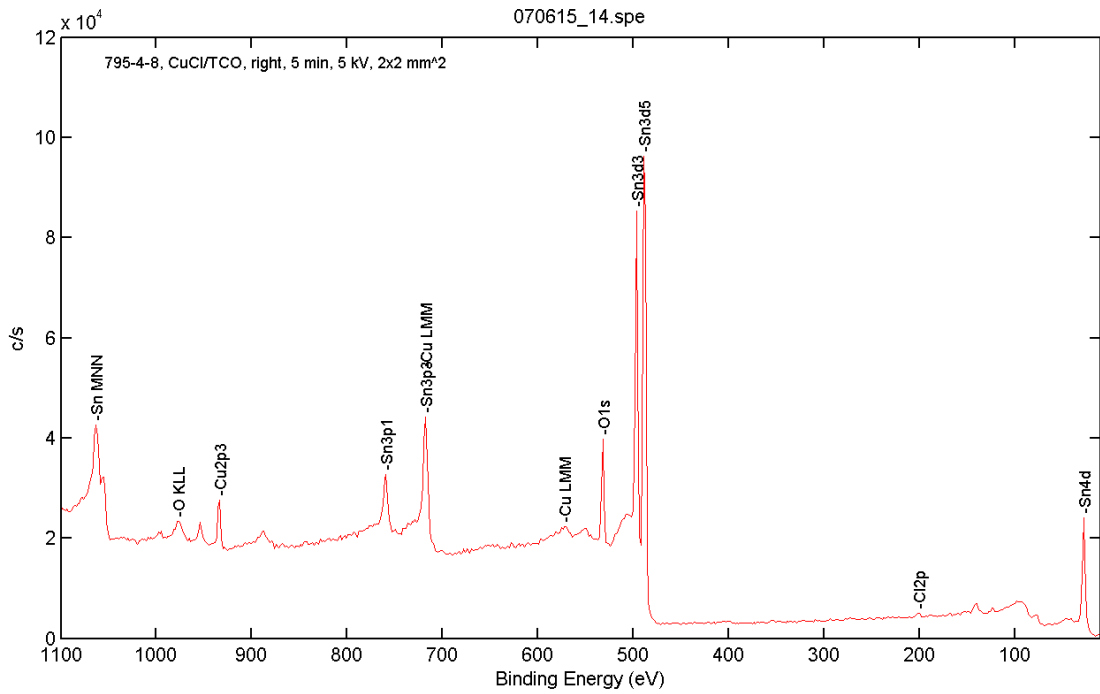


FIGURE A.1. TCO crater depth while unetched and etched with HCl

results, Figures A.2a and A.2b plot the arbitrary counts for a given binding energy of the surface material before and after Ar^+ sputtering, respectively. Referring to the $3d_{3/2}$ Sn (≈ 486 eV) and $2p_{3/2}$ Cu (≈ 932 eV) peaks of each plot it can be seen that during Ar^+ sputtering on the CuCl layer, the crater is formed deep enough into the layer that the majority of the crater bottom is made up of Sn and O (largest peaks in Figure A.2b). The Cu and Cl signal peaks are also significantly lower than before Ar^+ sputtering, indicating the effectiveness of the Argon Ion Beam etching technique to form a crater into both the CuCl and TCO layers.



(a)



(b)

FIGURE A.2. (a) Before and (b) after XPS measurements on the Ar⁺-sputtered CuCl/TCO layers.

APPENDIX B

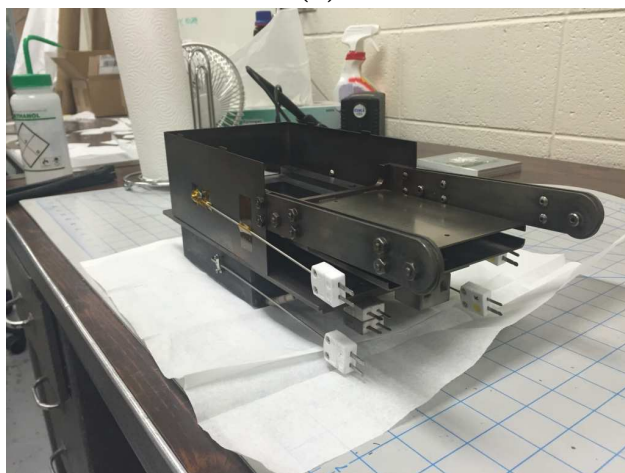
CSS DOMAIN THERMAL UNIFORMITY VERIFICATION

A crude thermal model was developed within the CuCl domain as a means for checking the thermal uniformity assumption across the substrate. The model was in correspondence with the thermocouple (TC) data collected during ARDS operation at source and substrate temperatures used for the full-well deposition experiments. After the top heater and bottom source reached steady-state in the system, TC values were measured in four locations in the CuCl domain. Two of them were placed on the SS304 side shielding that encased the upper half of the bottom source. This would measure temperatures of the side areas surrounding the substrate when the end effector was inserted into the sublimation domain. The remaining two TCs were mounted directly to the CuCl bottom source sides to verify that the source was also uniform. The TCs on the bottom source were both fastened with tiny nuts and bolts and secured with Kapton[®] tape to their locations as seen in Figures B.1a and B.1b. Measurements were taken 6 times at 2 minute intervals for statistical validation. The results at each source temperature are presented in Figures B.2a - B.2f. The overall trend of the data is that the side shielding had a 13-15°C change due to the open and anneal domains adjacent to the CuCl domain, as well as the 1°C difference for the CuCl bottom source walls. The large error bars on the bottom source TCs were due to the PID modulation and provide no other useful information.

A thermal model of the CuCl domain was created to calculate the temperature throughout the CuCl chamber region. Figures B.3a and B.3b provide a contour plot of the thermal modeling results when the TC data was obtained at bottom source and top heater temperatures of 192.5°C and 166.3°C, respectively. The plots show that the substrate does not see a



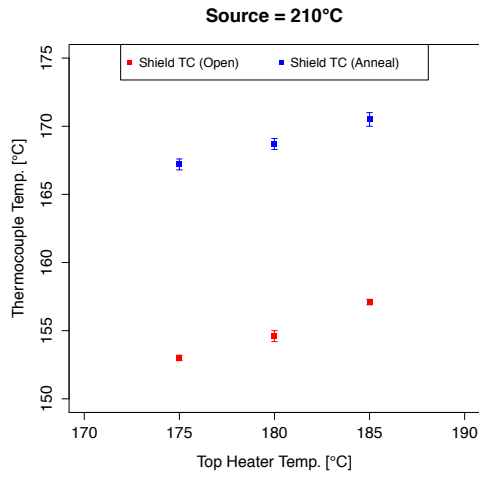
(a)



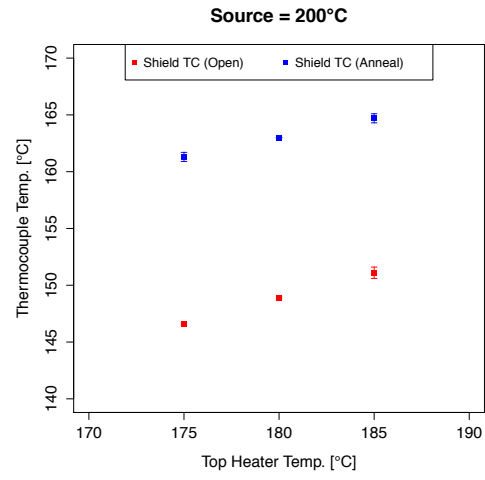
(b)

FIGURE B.1. (a) Side and (b) orthogonal view of the TC locations on the CuCl bottom source and side shielding

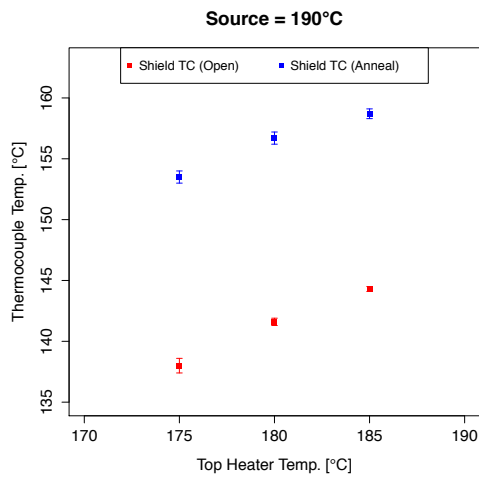
significant difference in temperature across its surface despite the 13-15°C gradient from the left-side shielding facing the open domain to the right-side shield facing the anneal domain. Temperature was measured using 100 points placed on the substrate bottom face line to determine the change in thermal conditions across it. As shown in Figure B.4, the maximum temperature difference across the substrate was only 0.2°C from the right to the left end, refuting the claim that a thermal gradient exists on the substrate.



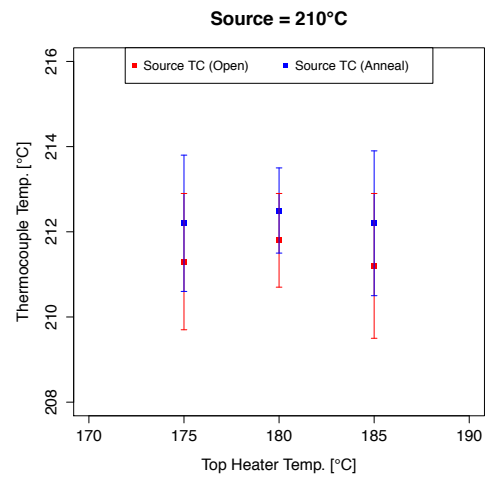
(a)



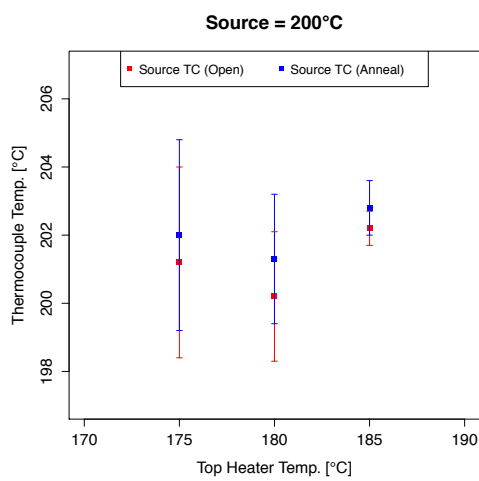
(b)



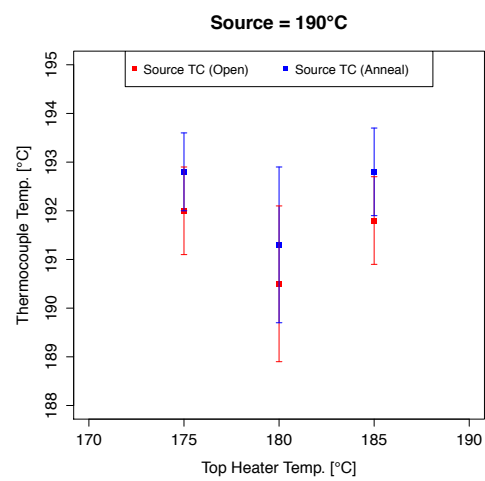
(c)



(d)

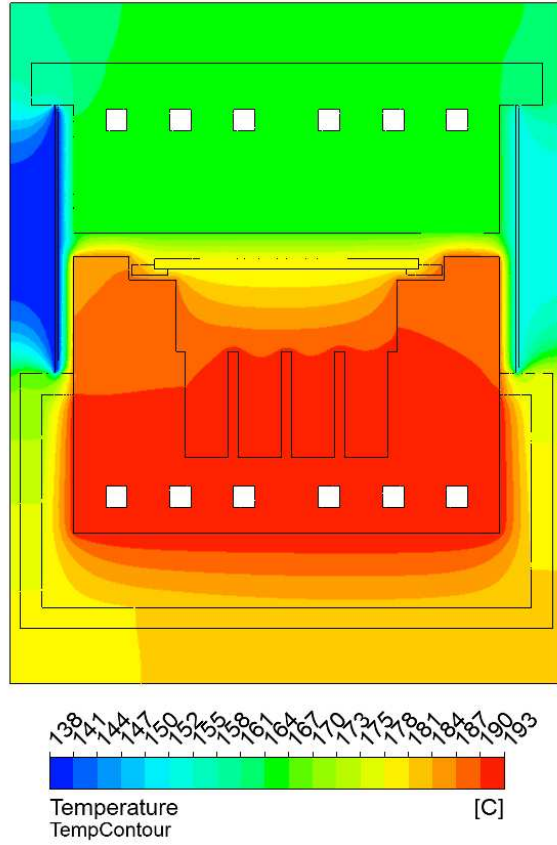


(e)

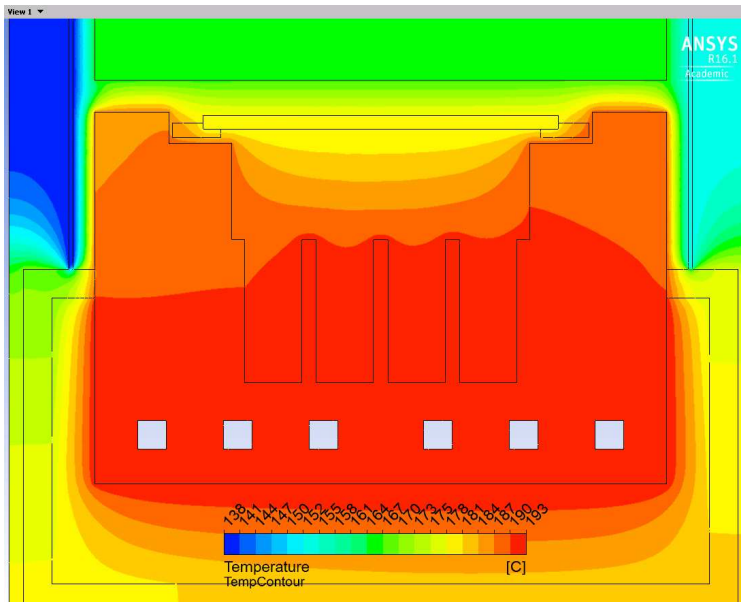


(f)

FIGURE B.2. Thermocouple data recorded for each source temperature



(a)



(b)

FIGURE B.3. (a) Full and (b) close-up contour plot of the CuCl domain when top heater = 166.3°C and bottom source = 192.5°C . The substrate temperature appears to be uniform according to the thermal model.

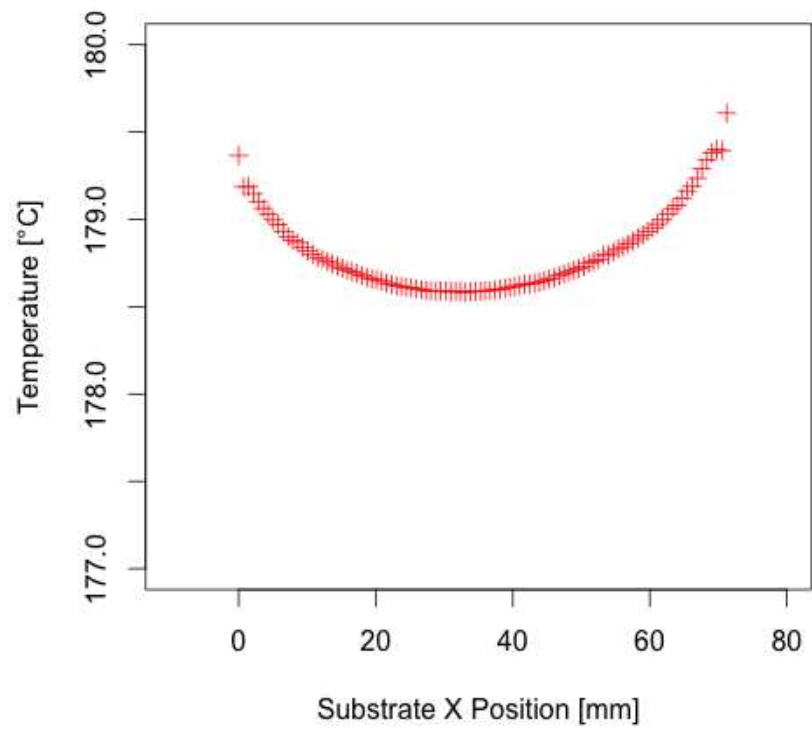


FIGURE B.4. Substrate temperature plot from the thermal model analysis

APPENDIX C

SUBLIMATION RATE PRESSURE DEPENDENCE

The theory of the sublimation rate [17] is fully expressed as follows:

$$(C.1) \quad \frac{dm}{dt} = A \cdot \sqrt{T} \cdot e^{\left(\frac{-\lambda}{RT}\right)} - S \cdot P \sqrt{\frac{M}{2\pi RT}}$$

where A is the pre-exponential factor, T is temperature of the gas, λ is the activation energy of evaporation, S is the sticking coefficient, P is the partial pressure of the gas, M is the molar mass of the gas, and R is the gas constant. It should be apparent from this equation that sublimation depends on both the rate of evaporation and the rate of condensation at the solid-gas interface. When the entire pocket containing the gas achieves an equilibrium vapor pressure condition, the sublimation rate is impeded ($\frac{dm}{dt} = 0$) and thus the expression becomes:

$$(C.2) \quad A \cdot \sqrt{T} \cdot e^{\left(\frac{-\lambda}{RT}\right)} = S \cdot P_{\infty} \sqrt{\frac{M}{2\pi RT}}$$

where P_{∞} is the vapor pressure of the gas. Therefore the sublimation rate can be redefined in terms of both temperature and partial pressure of the gas:

$$(C.3) \quad \frac{dm}{dt} = S \sqrt{\frac{M}{2\pi RT}} (P_{\infty} - P)$$

The sublimation rate used in this particular study for CuCl was represented as an Arrhenius rate expression (equation 2.2) that did not include the vapor pressure term P in order to study only the thermal aspects associated with sublimation and thin-film deposition. However, it was seen later in the research process that one of the main reasons the computational

model was not as accurate for the single-well case was to due to not accommodating the vapor pressure effects in the CuCl pocket domain. That is why a vapor pressure-dependent equation similar to equation C.3 needs to be somehow derived within the experimental sublimation rate data described in Section 3.2. Furthermore, such an equation needs to be applied to the simulation for improved accuracy in predicting the CuCl thin-film non-uniformities present across the substrate. This may require more sublimation experiments, in particular the single-well case instead of another full-well case, to see the differences in sublimation rate and how they relate to vapor pressure. This generalized expression would be an immediate benefit to the current simulation model and provide extra dimensionality to how ANSYS® FLUENT calculates the CuCl concentration in the mesh domain.